# The JUICE Radiation Environment Monitor, RADEM

Hajdas, Wojtek; Gonçalves, Patrícia; Pinto, Marco; Socha, Patryk; Marcinkowski, Radoslaw; Xiao, Hualin; Santos, Francisca; Arruda, Luísa; Menicucci, Alessandra; More Authors

**DOI**
10.1007/s11214-025-01163-9

**Publication date**
2025

**Document Version**
Final published version

**Published in**
Space Science Reviews

**Citation (APA)**
Hajdas, W., Gonçalves, P., Pinto, M., Socha, P., Marcinkowski, R., Xiao, H., Santos, F., Arruda, L., Menicucci, A., & More Authors (2025). The JUICE Radiation Environment Monitor, RADEM. *Space Science Reviews*, *221*(4), Article 43. https://doi.org/10.1007/s11214-025-01163-9

Space Science Reviews (2025) 221:43
https://doi.org/10.1007/s11214-025-01163-9

# The JUICE Radiation Environment Monitor, RADEM

**Wojtek Hajdas[1] · Patrícia Gonçalves[2,3] · Marco Pinto[4] · Patryk Socha[1,5] · Radoslaw Marcinkowski[1] · Hualin Xiao[1] · Francisca Santos[2,3] · Luísa Arruda[2] · André Galli[6] · Arlindo Marques[7] · Timo A. Stein[8,9] · Dirk Meier[8] · Beatriz Sánchez-Cano[10] · Elias Roussos[11] · Giovanni Santin[4] · Sam Verstaen[4] · Olivier Witasse[4] · Petteri Nieminen[4] · Nicolas Altobelli[12] · Laurent Desorgher[13] · Alessandra Menicucci[14] · Ingo Reinaecker[1] · Marina Vogiatzi[1] · Tigran Rostomyan[1] · Alankritaa Mrigatshi[15]**

Received: 20 June 2024 / Accepted: 26 March 2025


**Abstract**
The RADiation–hard Electron Monitor (RADEM) is an instrument on board the ESA JUpiter ICy moons Explorer (JUICE) deep-space mission launched on April 14th, 2023. As a part of the Cosmic Vision program, RADEM on JUICE will spend over three years exploring the radiation environment of the Jovian system, including its icy moons Ganymede, Callisto, and Europa. The instrument serves as an on-board radiation monitor, providing nonstop information on particle fluxes and their energy spectra. In addition to being a platform subsystem relevant to spacecraft safety and health, RADEM obtains scientifically valuable data on the radiation environment and extends the particle detection range covered by the JUICE Particle Environment Package (PEP) instrument suite to much higher energies, and broadens the energy coverage in the tens to hundreds of MeV range for electrons and protons, compared to past missions. RADEM consists of three detector subunits: the Electron Detector Head, the Proton & Heavy Ion Detector Head, and the Directional Detector Head. Each of them is connected to a separate readout electronics with a dedicated front-end Application–Specific Integrated Circuit (ASIC) designed especially for the JUICE mission. RADEM measures electrons in the 0.3–40 MeV energy range, protons in the 5–250 MeV energy range, and heavy ions within the Linear Energy Transfer range from 0.1 to 10 MeV cm mg$^{-1}$. The Directional Detector provides an angular coverage of incoming radiation up to about 35% of the sky. Being a platform device, the monitor operates and delivers data permanently. Therefore, RADEM measurements also cover the radiation environment of the interplanetary space during the mission cruise phase, including long-term studies of the environment between Venus and Mars as well as the detection of the Solar Energetic Particle events that propagate across different locations in the Solar System.

**Keywords** Space radiation · Detector technology · Jupiter · JUpiter ICy moons Explorer

## 1 Introduction

The Jupiter system, with the largest planet of our solar system, a plethora of icy moons, and a huge magnetosphere, still holds on to numerous mysteries. Only a few space missions

Extended author information available on the last page of the article

have been dedicated to the exploration of this fascinating world with just Galileo and Juno orbiting the planet so far. Despite the latest efforts with ground and space-based observations from telescopes such as JWST (Melin et al. 2024), in-situ observations are essential to understand the space environment of the Jovian system, particularly the radiation environment. Mission related constraints together with its duration and distance from Earth make it still very difficult to reach the planet. The JUpiter ICy moons Explorer (JUICE) mission (Grasset et al. 2013), part of the ESA Cosmic Vision program, is dedicated to unraveling scientific unknowns held by Jupiter. The Jovian system, consisting of the gas giant planet Jupiter itself, its magnetosphere, rings, moons, and neutral and plasma tori, can help us understand many working principles of space physics, including the process of planet and moon formation in our solar system (Fletcher et al. 2023).

The Jupiter particle radiation environment qualifies as one of the most extreme in our Solar System (Kollmann et al. 2018). Such a dangerous environment requires the implementation of enhanced radiation protection measures with much higher requirements on the radiation hardness of the spacecraft and its payload. The environment's extremity also poses a challenge to experimental measurements since instrument penetrating particles can trigger sensitive detector elements and degrade signal-to-noise. To prepare for this hard environment, the JUICE mission has applied extra precautions such as more shielding to all spacecraft subsystems and constant monitoring of the radiation levels. There are also two vaults designed to protect sensitive electronics. These precautions were the primary motivations for the development of the RADiation–hard Electron Monitor (RADEM).

It is also crucial to properly qualify all payload instruments designed for the Jovian system exploration, including validation of their operation in such a harsh environment already on the ground. This is particularly imperative for RADEM as a permanent monitoring device. Verification of its performance contains a characterization of its working concept, qualification in terms of the radiation hardness levels, and performance tests and calibration. Only thorough on-ground tests validated subsequently in space one can assure its best performance during the mission with its ability to collect full information on the Jupiter radiation environment with its dynamics and diversity.

Besides its role in spacecraft health monitoring, RADEM provides complementary science to the JUICE payload, with its unique capabilities to map the radiation environment of the Jovian system and its moons as never done before. The extensive energy, species and directional (pitch angle) coverage, coupled with the unprecedented spatial coverage of the inner magnetosphere achieved through the mission's trajectory, will bridge coverage gaps of past (Galileo) or ongoing (Juno) missions, add context to ground-based observations of the Jovian radiation environment and its long-term monitoring, achieve a comprehensive description of the local space weathering environment of Jupiter's icy Galilean moons, and provide unique insights into the radiation belts of Ganymede's mini-magnetosphere.

In this work, we describe RADEM's scientific objectives 2 with its general concept and main design features 3. In the next section we describe the modeling results of the instrument responses done firstly for verification and tuning during calibrations and later to generate RADEM response functions for unfolding particle spectra in space 5. Further we present results of qualification tests and particle calibration campaigns at the Paul Scherrer Institut (PSI) devoted to characterizing the instrument and optimizing its performance 4. Finally, we describe instrument commissioning and in-flight performance tests done shortly after the JUICE launch 6. We also include its first space data and discuss plans for multi-mission/instrument observations during the cruise phase as well as science goals and measurement scenarios of the Jovian system 7.

## 2 Requirements and Objectives

JUICE will encounter an extremely severe radiation environment of the Jupiter system, which has the most complex and energetic radiation belts of the Solar System and one of the most challenging space environments to explore and study in-depth (Anglin et al. 1992; Roussos et al. 2022). Although studied for many decades (Williams et al. 1992; Bolton 2017; Baker and Allen 1977; Allen et al. 1975), it has not been thoroughly characterized nor understood. During previous missions flying through the Jupiter radiation belts, a broad range of radiation effects of various significance were observed in the majority of the mission subsystems (Atwell et al. 2005; Fieseler et al. 2002). These radiation effects posed substantial risks of malfunctioning to various spacecraft and their sub-systems and payloads including even permanent performance deterioration. Therefore, the in-situ exploration of the hazardous environment of Jupiter's radiation belts poses many challenges in mission design, space planning, instrumentation, and development of state-of-the-art detectors.

As part of the JUICE spacecraft platform, RADEM offers the capability to monitor the spacecraft radiation environment that the spacecraft encounters as it flies across the solar system or as it surveys the Jovian magnetosphere. With a very short delay the JUICE operators and scientists are informed about potentially alarming radiation events, their associated risks, and their impact on science performance. RADEM, as a housekeeping instrument, is operating continuously to measure the radiation environment in situ. After pre-processing, these data are delivered to the spacecraft platform for further analysis. If the telemetry data packages indicate higher radiation levels, one can correlate them with potentially observed malfunctions of instruments and systems. It helps to define and apply protective measures to reduce radiation damage and performance deterioration of the mission and its science payload.

The RADEM operational objectives are to provide in-situ radiation environment data and extract useful, reconstructed particle spectra from its particle rate measurements. They will be applied to enhance various space weather services and improve the existing engineering models, allowing significant advances in our understanding of radiation belt systems. RADEM measurements will add up to generate complete data sets (i.e. with orbital, orientation and radiation data) from both cruise and in-orbit phases for multi-spacecraft analysis of the Jupiter and interplanetary space radiation environment. These objectives cover three main categories of radiation monitoring instruments: coarse housekeeping of the radiation measurements, support to platform and payload subsystems, and provision of preprocessed high level data for future projects and scientific analysis.

In addition, RADEM supports research of plasma and radiation environments, enhancing the quality of the data and scientific analysis. Scientific objectives of RADEM on JUICE can be split for the cruise phase lasting until the beginning of 2031 and the following 4 years nominal science phase during the orbit around Jupiter and Ganymede.

During the cruise phase, the main objectives of RADEM are:

- Optimisation of its spectroscopic output to maximize mission scientific outcome;
- Mapping the radiation environment between Venus and Mars, consequently identifying risks for manned missions;
- Measurements of Cosmic Ray fluxes and correlation of their behavior with solar events;
- Observation of Solar Energetic Particle (SEP) events, including time-resolved spectroscopy and angular distribution.

On the other hand, during the nominal science phase, the main goals are the:

- Contribution to the characterization of the Jovian radiation environment;

**Table 1** RADEM specification requirements

| | |
|---|---|
| Electron energy range | 0.3 – 40 MeV |
| Proton energy range | 5 – 250 MeV |
| Energy resolution | 8 log bins for electrons and protons |
| Peak electron flux | $10^9$ particles cm$^{-2}$ s$^{-1}$ ($E > 300$ keV) |
| Peak proton flux | $10^8$ particles cm$^{-2}$ s$^{-1}$ ($E > 5$ MeV) |
| Ion sensitivity | LET 0.1-10 MeV/(mg/cm$^2$) |
| Directionality | $E > 300$ keV; 28 directions |
| Particle separation | electrons, protons, ions (better than 90%) |
| Temporal resolution | at least 1 min |
| Mass; Volume | $< 5$ kg; $< 2000$ cm$^3$ |
| Power; Temperature | $< 3.6W$; $-40/+50$ °C |
| Data link budget | $< 70$ bps for science and housekeeping data |
| Autonomous operation | 7 days |
| Lifetime | 11 years |
| Radiation tolerance EEE parts | min 100 krad(Si) interior |

- Investigation of trapped particles spectra, composition, and directionality;
- Mapping of Jupiter's radiation belts, including how the Galilean moons influence the system;
- Studies of the environment dynamics establishing correlations with the magnetic field of Ganymede;
- Combined supporting observations with other science instrumentation obtaining in-situ data at lower particle energies (such as PEP; Barabash et al. 2025, this collection) to extend the energy range and enhance coverage.

These science goals highlight the importance of RADEM data during the whole mission duration. They will enhance solar particle propagation models, contribute to SEP studies and dosimetry risk analysis as well as provide detailed measurements of Jupiter particle environments, and extend data from other instruments to much higher energies. RADEM flux measurements are intended to be used to construct models of the radiation environment and optimize engineering practices for future missions.

To fulfill the above objectives, RADEM has been designed as a low mass and low power instrument with short bandwidth, and based on the set of requirements specified in Table 1. A dedicated, radiation–hard, Application–Specific Integrated Circuit (ASIC) VATA466 (Stein et al. 2016) was designed for RADEM front-end readout on JUICE by IDEAS (Integrated Detector Electronics AS)[1] with several contributions by the Paul Scherrer Institut (PSI) that helped to fulfill above requirements.

## 3 Technical Description

### 3.1 Concept

RADEM is a radiation monitor with a mass of 4.6 kg and a volume of 2 l. Since RADEM is outside the JUICE electronics vault, a large part of its mass was allocated for global

[1] https://ideas.no/.

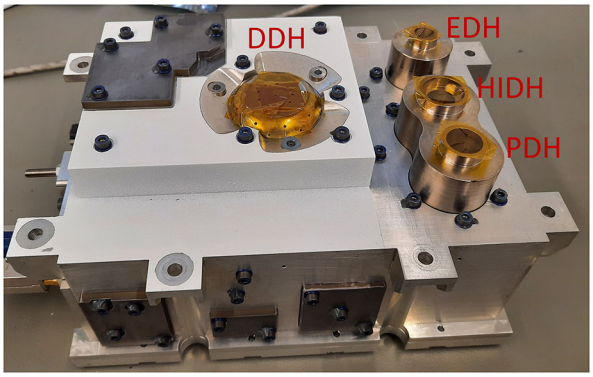


**Fig. 1** Photograph of the RADEM ProtoFlight Model with the Electron Detector Head (EDH), the Proton and Heavy Ion Detector Head (P&HIDH: PDH and HIDH), and the Directional Detector Head (DDH)

(thicker aluminum walls) and local (tantalum slabs) shielding. The instrument's average power consumption is below 3.6 W with the rush current within specification limits and zero power consumption when switched off. Survival heaters are switched on if the temperature drops below −30 °C.

To fulfill its requirements, RADEM is composed of three detector heads: the Electron Detector Head (EDH) with its Electron Stack Detector (ESD), the Proton and Heavy Ion Detector Head (P&HIDH) with its Proton Stack Detector (PSD) and Heavy Ion Stack Detector (HISD), and the Directional Detector Head (DDH) – see Fig. 1 (Pinto et al. 2019a,b; Socha 2021; Pinto 2019). The EDH and the P&HIDH consist of three (1+2) silicon diode telescopes – also named stack detectors. Several stack detectors have already been developed and flown in ESA missions. A few examples are the Standard Radiation Environment Monitor (SREM) (Mohammadzadeh et al. 2003), the BepiColombo Environment Radiation Monitor (BERM) (Pinto et al. 2017), and the Next Generation Radiation Monitor (NGRM) (Desorgher et al. 2013; Sandberg et al. 2022). RADEM's stack detectors follow the same working principle as these detectors: the higher the energy of a particle, the further it can travel into the stack. Particles are identified based on their deposited energy and hit signature in the diode's stack. Heavier particles generally lose more energy per unit of length (dE/dx). Different combination of energy and particle species may lose the same amount of energy in a layer, making their signatures ambiguous, i.e., electrons can be misidentified with protons and vice-versa. The exact number and position of the detectors and the necessary shielding of RADEM were adapted to the higher particle energies and fluxes expected in the Jovian environment.

The DDH is a novel detector designed at the Laboratory for Instrumentation and Experimental Particle Physics with a single diode (DDH). Its development was driven by the electron pitch angle anisotropies observed by the Galileo mission's Energetic Particle Detector in its tour of the Jovian system (Williams et al. 1992; Nenon et al. 2022). Since the EDH has a limited Field-Of-View (FOV), it may observe low or high electron fluxes depending on the spacecraft attitude and either neglect hazardous conditions or indicate very high particle fluxes in a relatively benign environment. By complementing the EDH with the DDH, RADEM will make precise electron environment measurements, allow the correlation of JUICE mission anomalies with radiation damage, and guide its operation during both the cruise and nominal mission phases.

Location of RADEM onboard of the JUICE spacecraft is presented in Fig. 2. One can see that the instrument's sensors have an unobscured field of view for particles coming from the top directions. Such location also provides better protection against radiation coming

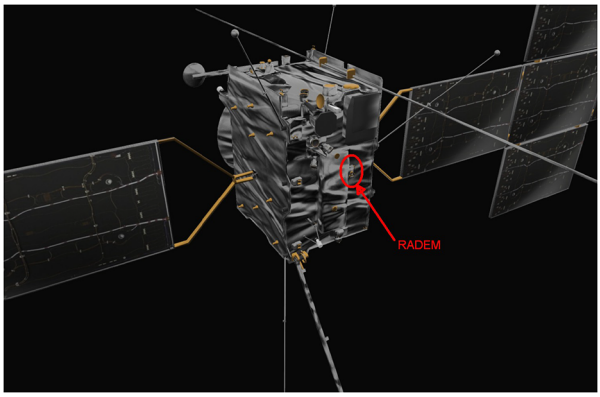


**Fig. 2** Location of RADEM onboard of the JUICE spacecraft

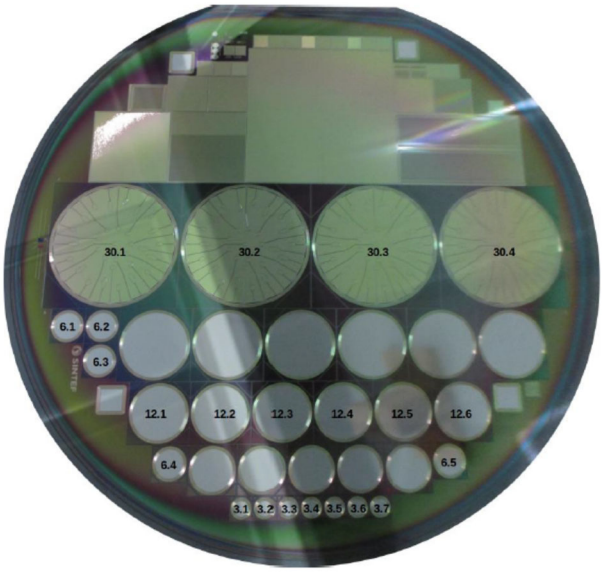


**Fig. 3** Si-wafer with all four RADEM diode types. Tracking numbers consist of their diameter and serial number (from Socha 2021)

from the back and, to some extend, side. It not only reduces the radiation damage but also improves RADEM response matrix capabilities by lowering the high energy background.

### 3.2 Active Sensors

The active parts of all detector heads are 300 μm thick, n-doped silicon diode sensors. These sensors were custom-designed by the Paul Scherrer Institute for RADEM and manufactured at SINTEF (Socha 2021). There are four different diode-diameters in RADEM: 3 mm, 6 mm, 12 mm for EDH and P&HIDH, and 30 mm for DDH, with 28 individual sensors for direction and 3 for background measurements. A wafer with all diode sizes can be found in Fig. 3. Full depletion was found to occur with a bias voltage of −35 V (Socha 2021). To consider radiation damage effects with an anticipated increase of the diodes' dark-current and ensure their full depletion until the end of the mission, the bias voltage of all diodes is set to −80 V.

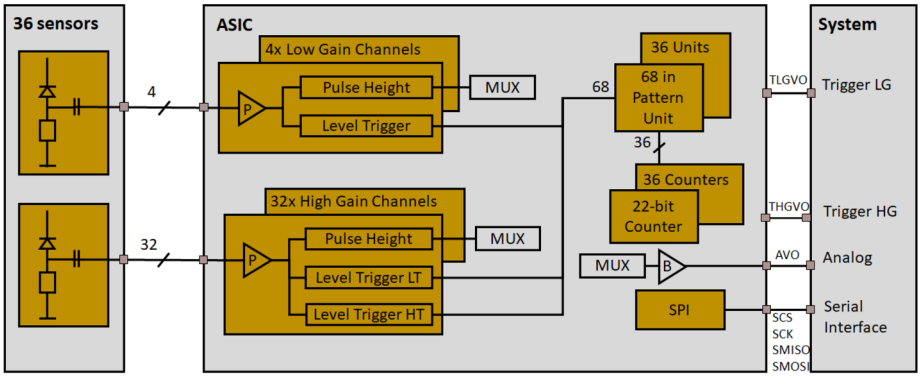


**Fig. 4** ASIC IDE3466 detector readout schematic (adapted from Stein et al. 2016). Sensors can be connected to either Low-Gain or High-Gain channels. In RADEM, both PSD and ESD are connected to High-Gain channels while the HISD is connected to Low-Gain channels

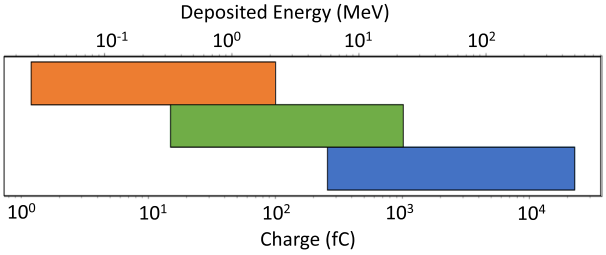


**Fig. 5** Dynamic range of the IDE3466 ASIC HGLT, HGHT, and LGLT channels in charge and MeV (converted using first principle calculations for silicon detectors). The three channels range overlap meaning that cross-calibration is possible between them

### 3.3 Front-End Electronics

RADEM's front-end electronics consist of three IDE33466 (VATA466) ASIC developed by IDEAS in Norway (Stein et al. 2016). Each detector head is connected to a dedicated IDE3466 ASIC unit. The ASIC has 36 input channels with charge-sensitive pre-amplifiers: four Low-Gain (LG), and 32 with High-Gain (HG) (see Fig. 4). While it is possible to perform pulse-height analysis, this feature is not implemented on RADEM due to its slow timing characteristics. The readout is made through its level triggers (thresholds) and then processed through 36 pattern units associated with one of its 36 counters. These and other ASIC circuits, such as the internal pulser are described in detail in Stein et al. (2016). Each of the 36 channels is split into a Voltage Analyzer (VA) and a Trigger Analyzer (TA) part. In RADEM, only the TA part is used. The TA part consists of one Low Threshold (LGLT) discriminator in the case of the LG channels, one Low Threshold (HGLT) discriminator, and one High Threshold (HGHT) discriminator in the case of the HG channels. Each threshold type has a different dynamic range that can be programmed through a 10-bit Digital-to-Analogue Converter (DAC) (see Fig. 5). The HGLT triggers with input charges from 1.2 to 100 fC (corresponding to $\sim 0.027$ MeV[Si] – $\sim 2.25$ MeV[Si]), the HGHT with input charges from 15 fC to 1 pC ($\sim 0.34$ MeV[Si] – $\sim 22.47$ MeV[Si]), and the LGLT triggers with input charges from 260 fC to 26.0 pC ($\sim 5.84$ MeV[Si] – $\sim 512$ MeV[Si]).

All thresholds are connected to a 36 pattern unit, each with a dedicated 22-bit counter. Individual patterns can be programmed using flag bits for all 68 thresholds (four from the LG channels and $64 = 2 \times 32$ from the HG channels). Two bits per threshold can be programmed, one to enable/disable the threshold in the mask, and the other to use the threshold

in either coincidence (higher than) or anti-coincidence (lower than) mode. The coincidence time can also be programmed globally from 50 ns to hundreds of ns, and the global gain of the ASIC can be tuned from 0.75% to 1.25% in case the environmental conditions or aging of the system justifies an adjustment. All settings and counter values can be written and read via a serial interface.

## 3.4 Stack Detectors

### 3.4.1 Electron Detector Head

The EDH consists of a single telescope with eight silicon sensors interleaved by aluminum and tantalum absorbers to degrade electron (particle) energies. The telescope without the front-end electronics is also referred to as Electron Stack Detector (ESD). Its main geometric characteristics are displayed in Fig. 6. All diodes are connected on a one-to-one basis to HG channels of a dedicated IDE3466 ASIC (each detector head has its ASIC). This way, all diodes can be programmed to work either independently (single coincidence mode), or in combination (multi coincidence mode) with the others. For example a coincidence between the first and the second detector diodes and an anti-coincidence with the third diode indicates that a particle went through the collimator, had enough energy to reach the first and the second diode, but its energy was too small to reach the third one. The purpose of the absorbers between the sensors is to help determine the energy ranges associated with each sensor. (Occasionally some electrons with energy sufficient to reach the next detector are scattered away e.g. in the absorber. Such effects are included in response modeling and verified during calibration runs.) To accommodate the large electron fluxes at Jupiter, 20 mm thick copper collimator limits the FOV to $\pm 7.5^{\circ}$. The collimator as a whole is also responsible for shielding the stack sensors from particles coming from side and bottom directions.

The collimator entrance window is made of a 0.4 mm thick aluminum slab (absorber). It serves to cut-off electrons below 350 keV and protons below 6 MeV. These are the lowest primary energies that can be observed by the first sensor. Energy cutoffs for each subsequent sensor is determined by the absorbers and sensors that precede it. The first principle calculations for both electrons and protons are given in Table 2. Electron energies in consecutive sensors follow a quasi-logarithmic scale from 0.35 to 35 MeV. Note that a large range of proton energies can also be detected by the stack. Generally, electron energy depositions are smaller than protons. This way, proton hits can be vetoed with the front-end electronics using a suitable value of the high threshold (HGHT) in anti-coincidence. All particles depositing in the sensor energies above the selected HT value are not accounted for. On the other hand, by increasing the HT thresholds, the EDH can also be used as a proton detector.

### 3.4.2 Proton and Heavy Ion Detector Heads

The P&HIDH comprises two particle telescopes, the Proton Stack Detector (PSD) and the Heavy Ion Stack Detector (HISD). Both stacks share the same ASIC unit. The PSD is constructed similarly to the ESD with eight silicon sensors interleaved by aluminum and tantalum absorbers (more details can be found in Fig. 6). The main differences are its larger FOV ($\pm 10^{\circ}$), tuned for the expected maximum proton flux (about ten times lower than the electron flux); a thinner, 0.2 mm thick aluminum absorber to measure lower energy protons; and the larger mass of the absorbers used to cover proton energies up to 250 MeV (see Table 3). All PSD sensors are connected to the HG channels of the ASIC. This means that, similarly to the ESD, the PSD can also be used as an electron detector.

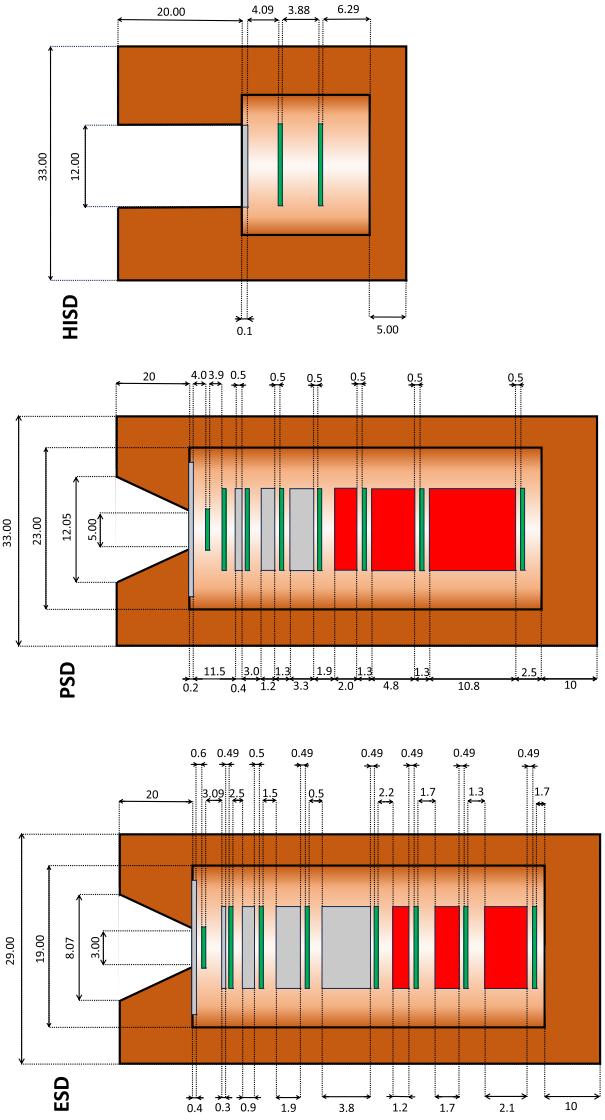


**Fig. 6** Side-cut view of the three detector stacks (Heavy Ion Stack Detector, Proton Stack Detector, and Electron Stack Detector); units are given in mm. Brown represents copper, gray aluminum, green silicon sensors, and red tantalum. All silicon sensors are 300 $\mu$m thick. (The opening angle of the cylinders as well as detector diameters are not in scale. ESD detector diameters are 1x3 mm (front) and 7x6 mm (rear), PSD - 1x6 mm (front) and 7x12 mm (rear), HISD - 2x12 mm)

As shown in Fig. 6, the HISD is a two-sensor telescope with a FOV of $\pm 45°$. Both sensors are connected to the LG ASIC channels as they only have a single lower threshold. Given the LG channel's relatively large dynamic range, the HISD can measure heavy ions from hydrogen to oxygen or heavier. However, the detector is limited by its single threshold per diode, which means that, depending on its threshold, it detects all elements above a certain mass simultaneously. Generally, the following detection patterns are possible: independent counting in each sensor, coincidence on one sensor and anti-coincidence on the other, and a coincidence between both sensors. Dedicating changing of thresholds and patterns makes it possible to focus on specific elements and energies. Such observations will be defined and tested during the mission. They will requires continuous and dedicated telecommanding of the instrument.

**Table 2** Electron and proton cutoff energies for each diode in the ESD. Adapted from Pinto (2019). Please note that for electrons a spread of detectable energies around the values in the table can be large

| Sensor | Electron energy (MeV) | Proton energy (MeV) |
|---|---|---|
| EDH 1 | 0.35 | 6.00 |
| EDH 2 | 0.50 | 12.5 |
| EDH 3 | 1.00 | 17.5 |
| EDH 4 | 2.00 | 25.0 |
| EDH 5 | 4.00 | 40.0 |
| EDH 6 | 7.00 | 50.0 |
| EDH 7 | 17.5 | 65.0 |
| EDH 8 | 35.0 | 80.0 |

**Table 3** Electron and proton cutoff energies for each diode in the PSD. Adapted from Pinto (2019). Please note that one can also tune the stack for limited detection of heavy ions while rejecting electron and proton hits

| Sensor | Proton energy (MeV) | Electron energy (MeV) |
|---|---|---|
| PSD 1 | 4.00 | 0.15 |
| PSD 2 | 9.50 | 0.45 |
| PSD 3 | 15.0 | 0.70 |
| PSD 4 | 25.0 | 1.5 |
| PSD 5 | 35.0 | 3.0 |
| PSD 6 | 50.0 | 10.0 |
| PSD 7 | 85.0 | >10.0 |
| PSD 8 | 125.0 | >10.0 |

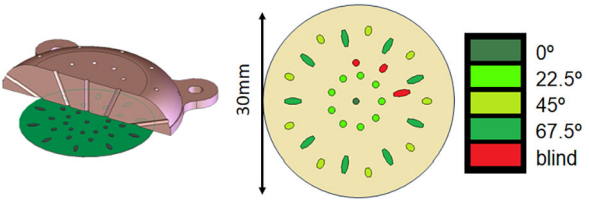


**Fig. 7** DDH cut-off side view (left) and sensor mapping (right). Adapted from Pinto et al. (2019b)

### 3.5 Directionality Detector Head

The DDH measures particles coming from 28 directions with a total FOV close to 1/3 of the sky. A single copper collimator, depicted in Fig. 7, determines the incoming directions. There are four zenith angles (0°, 22.5°, 45° and 67.5°), each with nine azimuthal directions (except 0°) (Pinto et al. 2019b). The active parts are 31 sensors placed as individual pixels on a single silicon wafer. Out of the 31 sensors, 28 are linked to a specific direction, each occupying an area equivalent to the projection of that direction in the plane. This means that there is a pixel size for every zenith angle. The remaining three pixels do not have direct access to space. Their function is to measure the background from high-energy penetrating particles. Each background pixel has a different area corresponding to the 22.5°, 45°, and 67.5° direction sensors. No background pixel exists for the 0° sensors since its area is very close to the 22.5° one (8% difference). All pixels are connected to HG channels of a dedicated IDE3466 ASIC (Stein et al. 2016). A 500 μm thick Kapton absorber was placed between the DDH collimator and the silicon wafer to cut off low-energy electrons. Since particles cross the absorber with different angles, the energy cutoff is different for each di-

**Table 4** DDH sensor information. Reproduced from Pinto et al. (2019b)

| Zenithal direction (°) | # of sensors (azimuthal directions) | Sensor area (mm2) | Electron energy cutoff (MeV) | Proton energy cutoff (MeV) |
|---|---|---|---|---|
| 0 | 1 | 0.79 | 0.30 | 7.00 |
| 22.5 | 9 | 0.80 | 0.30 | 7.00 |
| 45 | 9 | 1.20 | 0.35 | 8.50 |
| 67.5 | 9 | 2.18 | 0.50 | 12.5 |
| Blind | N.A. | 0.80-2.18 | 10.0 | 75.0 |

rection. The properties of the DDH are summarized in Table 4. A more detailed description of the detector sensitivity to Jovian electrons can be found in Pinto et al. (2019b), Pinto (2019).

## 4 Response Modeling

All modeling and simulations of RADEM responses for its detector subsystems were performed using the Geant4 v4.10.03 toolkit (Agostinelli et al. 2003). The modeling was an essential part of the instrument design phase to ensure that its construction fulfilled the requirements of the JUICE mission. The RADEM model was constructed in detail, including all critical electronic components and other relevant parts. It was updated during different phases of the instrument development e.g. including additional shielding protecting its readout electronics from damages induced by the radiation environment anticipated during the JUICE mission.

Therefore, the response functions of RADEM detector subsystems were computed with a fully representative instrument model. Crucial elements of the experimental setup used during instrument qualification and tests with particle beams and radioactive sources were also included when needed. Obtained responses provided a realistic depiction of RADEM performance with parameters such as detector thickness and active sensor area validated experimentally. All important electronic parameters, such as the minimum possible threshold values in the discriminators or the energy scaling coefficients, were also determined during the tests. It provided a path between instrument settings in physical units and their electronic equivalents. All calibration results from PSI exposure facilities were also validated with extensive simulations. Such steps were necessary to obtain reliable and accurate response functions. They were used to create the optimal configuration of RADEM as required for each particular operation phase in during the mission. Further simulations were performed to give responses of RADEM to the radiation environment as expected in space. They were based on existing models of Jupiter radiation (Jun et al. 2005; Santos-Costa and Bourdarie 2001; Divine et al. 2009) and served e.g. to determine the maximum anticipated counting rates or detector damage due to radiation.

### 4.1 Instrument Model

The RADEM mass model with its detector heads, mechanical components, and electronic parts was constructed based on the EFACEC[2] CAD file provided in the STEP format. To

[2] https://www.efacec.com/.

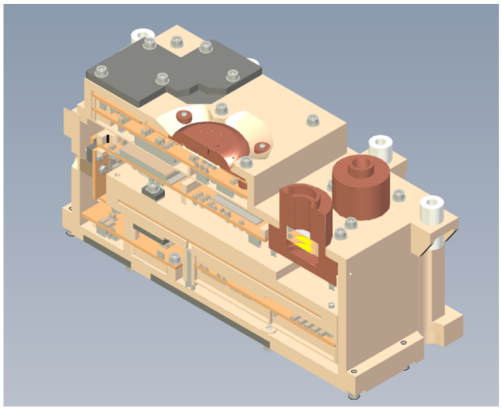

**Fig. 8** RADEM model cross-section illustrating level of details in simulations (from Socha 2021)

be used by the Geant4 simulation toolkit, a conversion from the STEP into the Geometry Description Markup Language (GDML) format was done using GUIMesh (Pinto and Gonçalves 2019). Precision levels of all model shapes were better than 0.01 mm. For the detector heads, a level of 0.001 mm was used. The RADEM GDML model, extracted with the Geant4 visualization tools, is shown in Fig. 8 using a cross-section depicting the interior. One can see that it contains not only precisely described detection subsystems and Si-diodes but also individual electronic components and additional shielding plates. Such a fully representative, detailed description was needed for an accurate response calculation and determining radiation dose levels in critical electronic parts. The results allowed for adding dedicated and least intrusive pieces of protective shielding. Simulations folded with the Jupiter radiation spectra specifications (Divine et al. 2009) enabled the optimization of local shielding plates and their thickness while minimizing the total mass of the instrument, as shown in the RADEM FM model in Fig. 1.

### 4.2 Experimental Setup

For a proper implementation and analysis of tests and calibrations in the lab and accelerator facilities, all such sides were added to the main model of RADEM as dedicated and separate GDML files. They included all such setup elements that might influence the experiment and, thus, the measured responses of RADEM. The new GDML models utilized tools from Hualin (2022) and contained relevant parts and materials of the experimental arrangement for each facility used during tests. In addition, the particle guns applied during simulations were defined according to the beam parameters of the facility used. Several different setup geometries were made available as presented in Table 5.

An example of the PIF experimental setup is shown in Fig. 9. One can see the ionization chamber on the right, the energy degraded made of Copper blocks in the middle, and a round Copper collimator on the left.

A simplified spacecraft geometry was also added for the final response generations to be used for the instrument onboard the JUICE mission. Its presence is less relevant for electron response functions but modifies protons and heavy ions responses for particles coming from the back plate of RADEM.

**Table 5** Models of test facilities and sources used for RADEM qualification

| Nr | Facility | Description |
|---|---|---|
| 1 | PIF | flat, monoenergetic, parallel proton beam in air, energy degrader, beam collimator, facility detectors |
| 2 | PiM1 | monoenergetic, initial parallel electron beam, air scattering, facility detectors |
| 3 | EMON | isotropic electron gun, spectrum defined by the slit, angular-limited electron beam in vacuum |
| 4 | radioactive sources | isotropic radiation source in air, specific spectra |

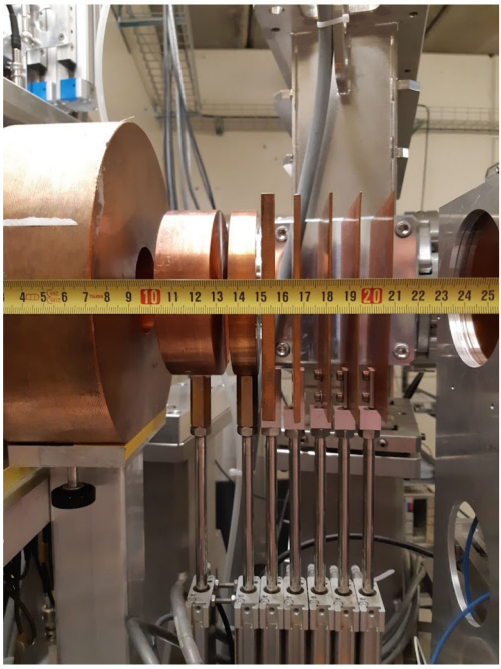

**Fig. 9** PIF experimental setup added to RADEM for calibration modeling

## 4.3 Response Functions

RADEM response functions are needed to unfold particle spectra from its channel counting rates. The Geant4 simulation model of RADEM was used to extract its response functions for the different types of incident particles as a function of their initial kinetic energy. In this process, protons and electrons with uniform energy spectra ranging between 5 MeV and 250 MeV, and 0.3 MeV and 40 MeV, respectively, were generated with isotropic angular distributions and $4\pi$ str solid angle. The contamination from particles with lower energies was tested, and such sub-threshold particles' impact on the final RADEM responses was found to be negligible for both protons and electrons (Socha 2021).

The outputs of the Geant4 RADEM simulation for each particle type are the energies deposited in each RADEM sensor, which are registered as a function of the particle's initial energy. The simulation output is then passed through RADEM signal processing chain and through a coincidence logic in the case of the detector stacks, and the corresponding channels are incremented. It should be noted that realistic energy thresholds applied to the

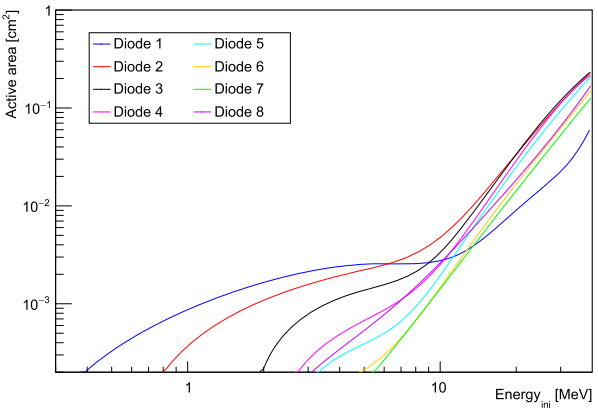


**Fig. 10** Effective area of the EDH diodes to electrons coming from $4\pi$ solid angle (from Socha 2021)

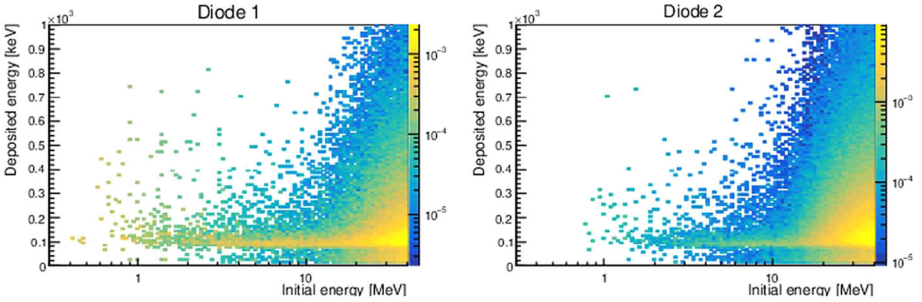


**Fig. 11** Energy depositions in the D1 and D2 EDH detectors for electrons coming from $4\pi$ solid angle with color scale normalized to the electron flux (from Socha 2021)

Si-sensors and the stack coincidence logic used during operation in space depend on the instrument noise levels and on the environment to which the detector response is being optimized. The thresholds for each channel can thus be adjusted in the process of detector calibration and signal-to-noise ratio optimization. One can also test and adjust the coincidence logic. The impact of the sensor energy thresholds and coincidence logic settings in the particle detection efficiency is thus taken into account in its response functions in every update resulting from the calibration of the detector.

### 4.3.1 Electron Response

The EDH response to omnidirectional electrons with no coincidence logic applied is shown in Fig. 10. One can see that new channels become active with increased electron energies and that electrons with energies above 10 MeV leave signals in all sensors of the EDH stack. The values of lower thresholds were all set to 50 keV. The effective area showed in the figure represents detection probability for fluxes equal to 1 electron per $cm^2$.

Realistic threshold values and coincidence logic should be applied to the pulses in the ASIC channels corresponding to the signals in each Si-sensor to obtain response functions for electrons. To determine threshold values, electron signals in the Si-sensors must be discriminated from noise and signals left by protons and other particles. Energies deposited by electrons in the 2 first sensors of the EDH stack are plotted against initial energy and deposited energy in Fig. 11. The color scale in the figure shows detector responses normalized

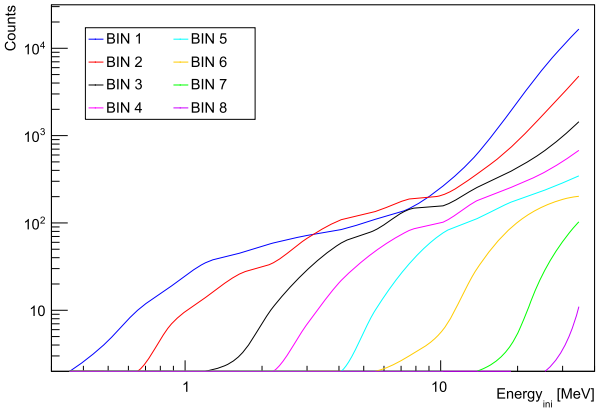


**Fig. 12** Electron response function for EDH with applied coincidence logic (from Socha 2021)

to the electron flux at a given energy. Most depositions cover the region between 50 keV and 300 keV. This energy range defines the conditions for setting HGLT and HGHT discriminators in the coincidence logic. The value of HGLT cuts off the region below the noise level, while the value of HGHT is tuned to reject proton contamination from each electron channel. As during factory qualification one realized that the instrument noise levels are higher than anticipated we should note that the final response matrices can only be determined after on-ground calibrations and its further verification and optimization during calibrations in space.

After setting thresholds in all sensors, a coincidence logic between the signals in the stack is applied. It attributes combinations of hit sequences in the stack to electron energy channels. It obviously takes into account the fact that electrons with higher energies reach deeper sensors of the stack. The results for the EDH response functions to white spectrum of electrons coming from all directions are obtained using a coincidence matrix corresponding to the EDH initial specifications (i.e., all LT = 50 keV and all HT = 300 keV and coincidence matrix using a linear pattern of coincidences with the last detector set in an anti-coincidence mode). The counts corresponding to the real response matrix are shown in Fig. 12 as a function of energy for a flat energy spectrum of $10^5$ electrons per (MeV cm$^2$ sr). The corresponding 2D responses binned for the 8 logarithmic energy intervals are shown in Fig. 13, representing the detection probability in each bin for a flat electron spectrum per (MeV cm$^2$ sr). One can see that RADEM shows clear sensitivity to low energy electrons with sequential opening of its spectroscopy channels to higher energy values.

### 4.3.2 Proton Response

Figure 14 displays PDH response to protons with no coincidence logic applied. One can see values of proton energies needed to reach each sensor (Si-diode) of the detector stack. Protons with energies higher than 70 MeV cross the full stack, reaching its last Si-sensor. It is also shown that around this energy value, the shielding of the telescope becomes transparent, and detectors can be hit from any direction.

To obtain the response functions for protons, the HGLT and HGHT discriminator values were chosen, studying the distribution of energies deposited in the Si-sensors. Figure 15 shows the energy deposited in the first 2 sensors of the stack as a function of the energy of the incoming protons. One can see that for very high proton energies, their energy depositions in the 300 $\mu$m thick Si-sensors are largely between 250 keV and 300 keV. For lower energy

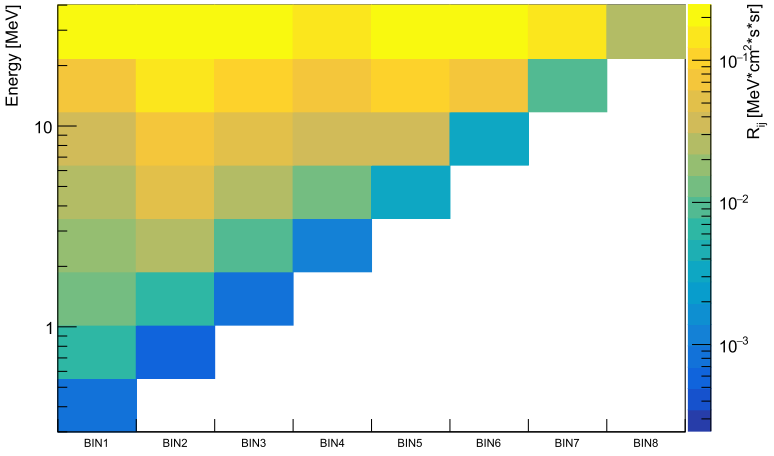


**Fig. 13** 2-dimensional electron response function for EDH for 8 energy bins (from Socha 2021)

**Fig. 14** Effective area of the PDH diodes to protons coming from $4\pi$ solid angle (from Socha 2021). Only the LT values of 300 keV and no coincidence logis were applied

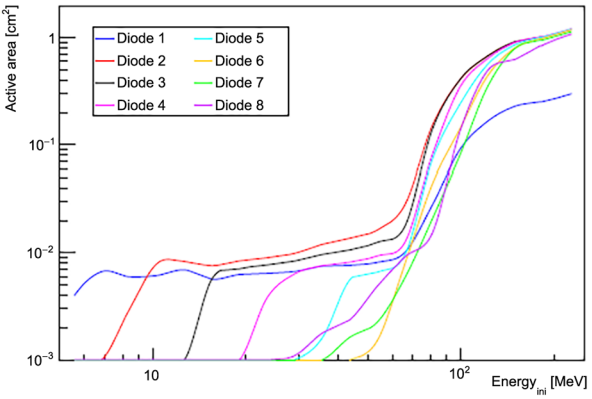


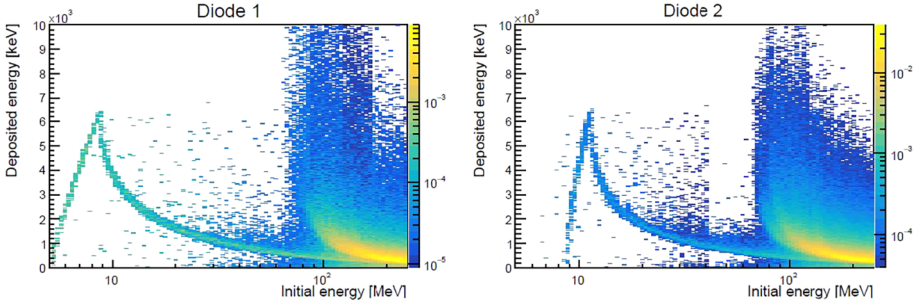


**Fig. 15** Energy deposited in PDH detectors D1 and D2 for protons coming from a $4\pi$ str solid angle (from Socha 2021)

protons stopping inside the sensors, deposition values are higher reaching more than 6 MeV. In the higher energy region, starting around 80 MeV, one can see signals with very large energy depositions. These events come from energetic protons hitting the sensors through

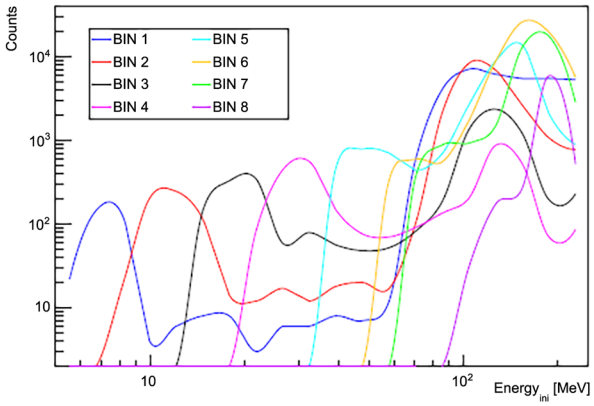


**Fig. 16** Proton response function of PDH with applied coincidence logic (from Socha 2021). The coincidence scheme use chain of sensors in coincidence ended with the last sensor set to anti-coincidence

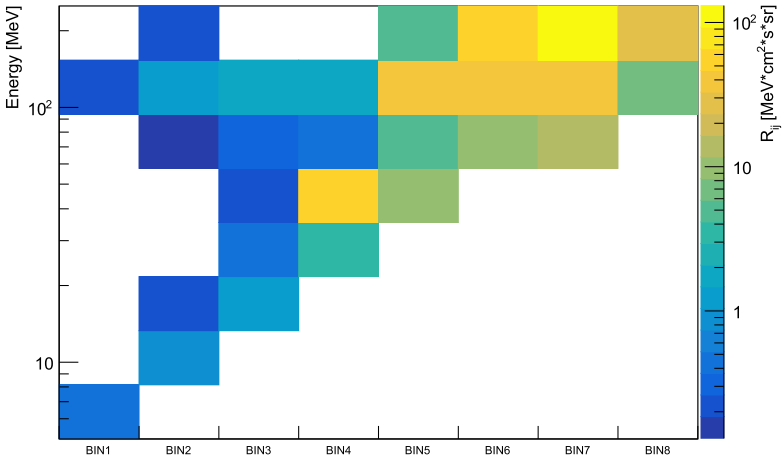


**Fig. 17** 2-dimensional proton response function of PDH for 8 energy bins (from Socha 2021)

the shielding i.e. outside of the collimator aperture. They cross the detector at large angles, enabling much higher energy depositions. Such unwanted detections form a background that can be removed by setting appropriate values for the LT and HT discriminators and applying proper coincidence logic. It also allows for a very clear separation of protons from electrons. One uses the HT discriminator in the positive coincidence logic for a unique proton identification. Data shown in the figures were obtained with energy thresholds above 500 keV, effectively selecting only protons stopped inside the detector. The LT discriminator is typically set slightly above electron pulses (in ideal case at 300 keV). Adding to it a further coincidence pattern between several stack diodes allows for both selection of proton energies and removal of signals from both electrons and high-energy particles coming through the shielding. The computed proton response functions in PDH as a function of the proton initial energy are shown in Fig. 16. The 2D responses given as bins for eight logarithmic energy intervals are presented in Fig. 17. As noted above, the instrument noise levels were higher than anticipated. Nonetheless, it turned out that their impact on proton responses was smaller than for electrons due to already high values of the threshold applied for proton detection.

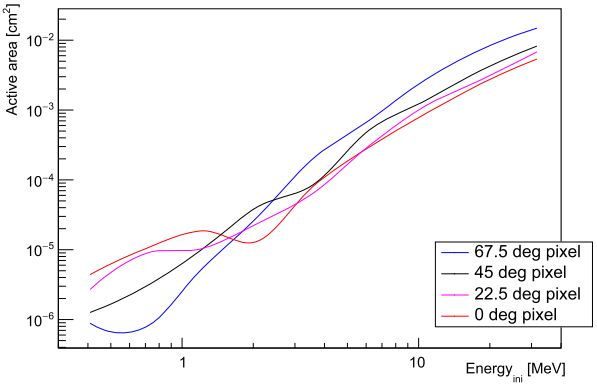


**Fig. 18** Effective area of the DDH diodes to electrons coming from $4\pi$ (from Socha 2021)

The responses presented in the figure present clear opening of consecutive channel with proton energy.

It should be noted that both the EDH and the PDH detectors can be tuned to detect protons and electrons, respectively, using different combinations of threshold values and a modified coincidence logic. However, their performance is optimal for the corresponding particle type to which they were optimized, namely due to the choice of the thicknesses of the absorbers that separate the Si-sensors in each stack.

### 4.3.3 Directionality Response

Figure 18 shows the directional detector active area for an omnidirectional electron flux as a function of energy for pixels covering its four zenith directions. The values were obtained using the values of LT=50 keV for channels. The effective area of the DD sensors is given by their surface of about 1 mm$^2$ and solid angle opening of 7.5°. It can be seen that the signal increases continuously for all directions for electron energies of about 3 MeV and more. This is due to shielding penetration and particles reaching the silicon wafer after crossing the instrument structure including top collimator. It is expected to improve responses by optimizing range of accepted energies after calibrations on-ground and in space. It is specially valid for electrons for which higher noise levels were observed.

The directionality detector works as a set of counters incremented using the acceptance range between the LT and HT discriminators. Its sensitivity covers electron energies starting from 300 keV upwards. The contamination with higher energies, as shown in Fig. 18, begins around 3 MeV, defining its effective energy range (Pinto et al. 2019b). For detections of electrons, the LT is set above the noise level, while HT can be used to cut off higher depositions, e.g., from proton events. As in the case of the RADEM telescopes EDH and PDH, the directionality detector DDH can be set up to detect protons by applying properly adjusted settings to its thresholds.

### 4.3.4 Heavy Ions Response

With only two Si-diodes and two counters making the heavy ion telescope, the response of this telescope is rather simple. The heavy ion telescope can be tuned using only two discriminators. Thus, only two predefined threshold LET values can be defined for passing heavy ions to detect their flux. They can be set to cut off the noise and even pin down energy depositions from selected heavy ions. The coincidences can be used to limit the field of

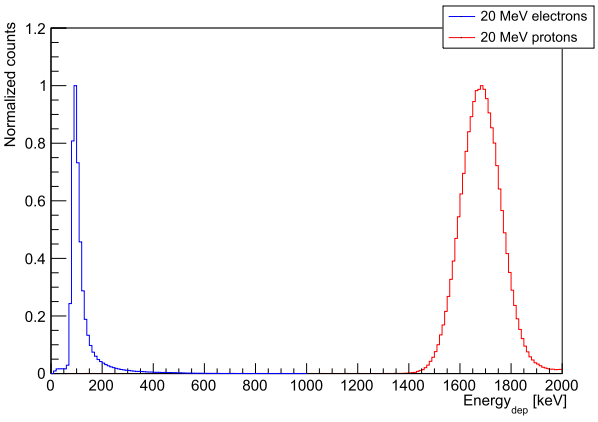


**Fig. 19** Energy depositions for 20 MeV electron and proton in the EDH detector (from Socha 2021)

view for the incoming particles. They also help remove signals from particles crossing the instrument from the side.

### 4.3.5 Particle Separation

To distinguish electrons from protons or heavier ions, a set of energy discriminators is applied to the signals of all Si-detectors, as described in the previous sections. As already mentioned, the readout electronics apply two discriminator levels (LT and HT) to signals coming to the ASIC input from a Si-detector. Logical pulses coming from the full set of active ASIC discriminators have a dual purpose. Firstly, they allow the selection of energy limits of the detected particle, attributing them to a proper energy bin. For both the PDH and EDH telescope or stack, there are eight such energy bins. According to the instrument design specifications in Table 1, they are predefined for either protons or electrons with a possibility for a redundancy (role swap). Secondly, discriminators also prevent signals from different particles from being detected inside the same energy bin. The discriminator logic can thus be applied as a veto (anti-coincidence), helping to set upper energy limits for the incoming particles in each energy bin or channel.

In the electron telescope EDH, the LT discriminators separate particle signals from detector noise. The HT discriminator removes signals from energetic protons and ions. In the proton telescope PDH, the LT discriminators are set high enough to cut off most signals from electrons. The HT discriminators select protons with large energy deposits specific to the particular energy bin. Discriminators in the directionality detector DDH can be tuned for either electrons, protons, or both. The rules are similar to the electron telescope. An example of typical energy deposits from electrons and protons with energies of 20 MeV is presented in Fig. 19. The discriminator set between two energy peaks from electrons and protons clearly separates the corresponding signals.

For heavy ions hitting the electron or proton telescope, the selection of coincidence conditions combined with the discriminator settings reject them from being observed. The heavy ion telescope uses only one discriminator per Si-detector and allows for simple coincidence between two sensors. It is sufficient to use it for removing contamination from both electrons and protons hits in these heavy-ion channels.

**Table 6** List of calibration facilities at PSI

| No | Facility | Location | Particle | Remark |
|---|---|---|---|---|
| 1 | Source lab | EMON | $\beta$ and $\gamma$ | noise scan |
| 2 | Proton Irradiation Facility | PIF | protons (E$\geq$ 6 MeV) | area, threshold scan |
| 3 | Electron monochromator | EMON | $\beta$ (E$\leq$ 2.2 MeV) | energy scans |
| 4 | High energy electrons | PiM1 | $\beta$ (E$\geq$ 10 MeV) | energy scans |
| 5 | Source lab | EMON | $^{90}$Sr collimated | DD map, patterns |
| 6 | Proton Irradiation Facility | PIF | protons (E$\geq$ 6 MeV) | energy scans |

## 5 Calibration

For reliable determination of particle spectra in space, two RADEM models, EM and FM, were calibrated on-ground. To ensure the best performance characterization and instrument tuning, all runs used particles, their energies, and fluxes as anticipated during the nominal operation in space.

All calibration tests with the FM were performed at PSI. The Table 6 lists the facilities used to characterize the instrument.

The applied procedures enabled the determination of the real RADEM performance. It also allowed for comparison of its features with the instrument requirements. This section contains a calibration description, presents the results, and includes consequential plans for the near-Earth commissioning phase and space calibrations.

### 5.1 Objectives of the Calibration

RADEM was initially characterized by its noise levels and subsequently exposed to predefined beams of electrons and protons. The particle runs are aimed at verifying the requirements put on the instrument. The process encompassed checking energy ranges and energy binning to detect electrons and protons, confirming the maximum detectable fluxes of both particles and the ability to distinguish between them. In addition, one should characterize RADEM with heavy ions. The heavy ion tests were performed with the breadboard (BB) model only, using heavy ion beams at the HIMAC - NIRS institute in Chiba, Japan.

### 5.2 Intrinsic Noise Levels

Noise levels were measured for each sensor, i.e., the Si-diode in all three detector subsystems. Threshold settings are quantified in units of Digital to Analogue Converter (DAC) channels directly mapped to the values in units of fC using ASIC manufacturer information. One of the goals of the calibration was to verify this mapping and provide each sensor with the real, verified conversion factors between the threshold value (DAC units or factory fC) and deposited energy (in keV). Noise measurement scans and set threshold values were done for all Si-diodes in EDH, P&HIDH, and DDH detection subsystems. The lowest noise values (represented in DACs channels or factory fC) were found for the DDH and were equal to about 10 DAC units using the LT thresholds. Slightly higher values of about 13 DAC units were found for the LT EDH. The highest values of about 35 LT DAC units were measured for the PDH. The HT discriminators had their noise similar to or even higher than the LT ones. It was less relevant as their values during normal operation are always much higher than the LT. It was also observed that some sensors had their noise level slightly higher

**Table 7** Noise counts example for EDH sensors

| Sensor | Low threshold | Counts in 15 s |
|---|---|---|
| 1 | 13 | 4 |
| 2 | 13 | 0 |
| 3 | 13 | 4 |
| 4 | 13 | 1 |
| 5 | 13 | 1 |
| 6 | 13 | 1 |
| 7 | 13 | 2 |
| 8 | 13 | 2 |

than the rest. It had to be cut off, increasing the corresponding discriminator thresholds. An example of the noise level counts for 15 s measurement in the EDH is given in Table 7.

### 5.3 Effective Area

The effective area was measured for each sensor in the EDH, PDH, and DDH subsystems. One used a flat field proton beam with an energy of 200 MeV. The geometrical area was compared with the measured one, which was determined by the precisely known proton flux and counts in the sensor detected based on energy depositions. The threshold values settings were 35 DAC units (factory fC) for PDH, 15 DAC units for EDH, and 11 DAC units for DDH. The determined effective area for all sensors was always lower than the geometric one. For example, the effective area values for the EDH were on the level of about 40% of the geometrical one. The lowest ratio was found for the top detector. Variability between sensors was roughly on the level of 20%. These results indicated that the threshold values set to cut-off the high level of noise had an impact on particle detection efficiency (see details in the following sections). Generally, noise levels strongly depend on temperature and their subtraction results in large uncertainties and lower detection efficiencies for particles that deposit less energy. The response matrices therefore must be generated for each energy separately depending on the specific threshold value. Energy depositions that were inside the noise level could not be detected. As a consequence, the detection efficiency of such sensors was smaller. Compared with the energetic protons detection efficiency of about 40%, electron detection will be even less efficient as they deposit less energy than protons. For the case of the PDH, the effective area was found to be on the level of only about 30% of the geometrical one. The best results with the highest ratio were determined for the DDH sensors with values between 60% and 95%. As the measurement was done with protons coming through the shielding, the effective energy on the sensor was equal to about 70 MeV. Such protons have much higher energy depositions in the sensor, and the results require corrections before further conclusions about the cut-off noise values are drawn. In addition, as the DDH is used for measurements of radiation angular distributions, such large efficiency variations require careful modeling to prevent systematic errors for space data analysis. The comparison between the geometrical area and the effective area measured for the EDH with 200 MeV protons is presented in Fig. 20.

### 5.4 Calibration Coefficients

Determination of the calibration coefficients for the threshold settings was done during RADEM exposures to the mono-energetic protons with predefined energies. The well-known

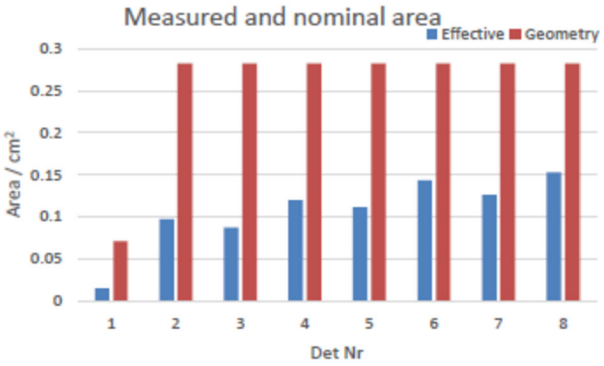


**Fig. 20** EDH nominal and effective area measured with a flat beam of 200 MeV protons

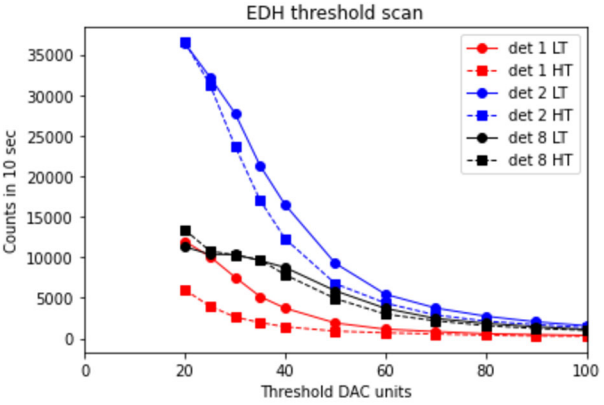


**Fig. 21** Scans over the lower and higher thresholds for selected EDH sensors using 125 MeV proton beam. Data points below 20 DAC were omitted because of high noise level at low DAC values

energy depositions were tested with threshold scans for either LT or HT discriminators. This allowed us to obtain the keV to DAC value (factory fC) coefficients for all RADEM detectors. All thresholds were scanned over the whole LT and HT DAC ranges from the noise level (i.e. the minimum values at which the detector had no counts without the beam) to the DAC value of at least 100. For this purpose, RADEM was configured for the single coincidence mode counting using a proper threshold discriminator, i.e. either LT or HT, attributed to the corresponding detector counter. An example of the threshold scans for the energy of 125 MeV is shown in the Fig. 21 for selected EDH detectors (1,2 and 8) and LT and HT discriminators. One can see differences between LT and HT scans indicating deviations from the factory data sheet. For both cases, there is also a lack of saturation level caused at low DAC values due to high noise levels. Therefore, deriving calibration factors was done individually for each channel and its discriminators. It was more complex and prone to larger uncertainties. The final results relied on realistic Monte Carlo simulations performed with a representative model of the proton beam facility and an exact model of the RADEM detector heads. The effective area curves in the function of the energy threshold from the simulations are presented in Fig. 22.

The calibration coefficients to convert DAC to keV were obtained by matching the measured and modeled effective area curves. The plateau level could not be reached (except for two channels), so using it for the determination of the inflection point (the average energy loss) of the curve was impossible. Finding the coefficients for HTs was more difficult as their noise levels were higher than for LTs, which reached values of about 20 DAC units.

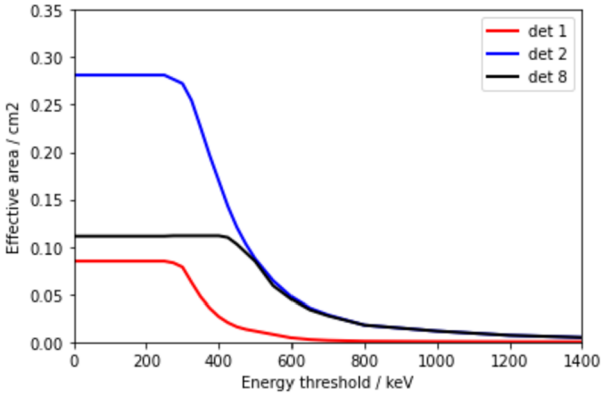


**Fig. 22** Response simulations of EDH sensors 1, 2 and 8 for 125 MeV proton beam

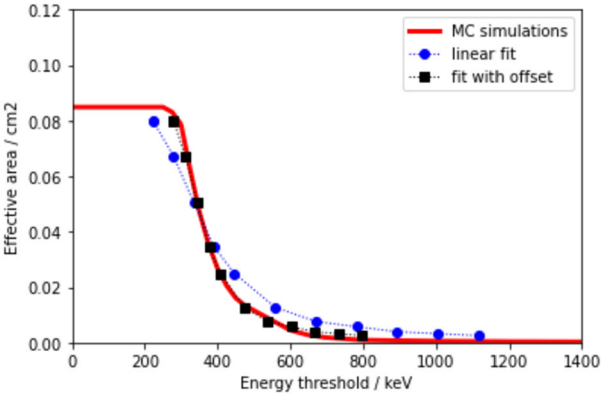


**Fig. 23** Linear fit example of simulated and measured threshold scans the EDH detector 1

Therefore, the values of the calibration coefficients keV to DAC for the HT were derived from comparing the counting rates between LT and HT threshold scan curves, with 20 DAC being the lower limit for these scan curves. An example of fits used to get the calibration factors is presented for the EDH detector 1 in Fig. 23.

In the case of the PDH, we also used protons of 50 MeV, which deposited much higher energies in the sensors than 125 MeV ones. Unfortunately, for the 50 MeV protons only first detectors were hit and also for them the threshold scan curves were far from reaching the plateau levels due to higher noise values in the PDH. Therefore, the determination of the calibration coefficients relied fully on the modeling and comparisons using the rate-matching scheme as already applied for the EDH.

For the DDH sensors, the noise level of around 10 DAC units for all LT discriminators allowed for similar analysis and matching as in the case of the EDH. The noise levels were similar for the HT, but the scan curves and thus calibration factors were very different. Once again, for HT scans, no plateau could be observed while for LT the plateau region was very narrow. Therefore, the rate matching scheme between LT and HT threshold values of the DDH had to be used.

The final results are presented in Table 8 for EDH (electrons) and in Table 9 for PDH (protons). Typical values in EDH for LT are around 11 keV/DAC with a standard deviation of about 1.1. The HT values are higher, with a mean factor of about 13.3 keV/DAC and a standard deviation of almost 2.0.

**Table 8** Conversion factors for EDH LT and HT discriminators

| Sensor no | LT conversion keV/DAC | HT conversion keV/DAC |
|---|---|---|
| 1 | 9.75 | 12.1 |
| 2 | 10.3 | 11.4 |
| 3 | 10.8 | 11.1 |
| 4 | 10.2 | 14.6 |
| 5 | 11.0 | 15.2 |
| 6 | 10.8 | 12.6 |
| 7 | 12.1 | 15.9 |
| 8 | 13.2 | 13.1 |

**Table 9** Conversion factors for PDH LT and HT discriminators

| Sensor no | LT conversion keV/DAC | HT conversion keV/DAC |
|---|---|---|
| 1 | 5.48 | 6.00 |
| 2 | 4.95 | 7.23 |
| 3 | 4.90 | 9.04 |
| 4 | 4.81 | 6.26 |
| 5 | 4.98 | 6.53 |
| 6 | 5.24 | 7.67 |
| 7 | 5.24 | 5.23 |
| 8 | 6.94 | 12.4 |

The analysis made during the threshold scans allowed for the determination of realistic noise levels in RADEM subsystems. The lowest values of around 150 keV were found for the EDH. The PDH showed higher noise levels of about 180 keV, while the highest noise of about 200 - 220 keV was seen in the DDH. Thus, the DDH subsystem has the lowest efficiency for detecting electrons. These results corrects for the lowest noise levels exhibited in the DAC units based originally on the instrument data sheet where 1 DAC unit was equal to 1 fC.

Having determined both the calibration coefficients and noise levels, we could established realistic LT and HT threshold values in the sensors. We optimized them for the best rejection of the noise as well as highest level of proton separation in the EDH and DDH and electrons separation in the PDH. The proposed initial EDH threshold settings with an LT value of about 150 keV and an HT value set to 5000 keV. The proposed initial PDH threshold settings with an LT value of about 180 keV and an HT value set to 5000 keV. The settings applied in the DDH subsystem correspond to the LT value of about 220 keV and the HT value of 5000 keV. Such settings, were initially applied in space for EDH, PDH, and DDH. The did not provide any electron-proton separation yet and were used rather to allow for a better preparation of in-space calibrations. The single value of the LT discriminator in the HIDH is set to 1100 keV only. It clearly allows for contributions from the Cosmic Ray protons also simplifying the future in-space calibrations.

### 5.5 Electron Energy Scans

Electron responses in the function of particle energy were measured using two radiation facilities: radioactive sources in the EMON monochromator and high-energy beams in the

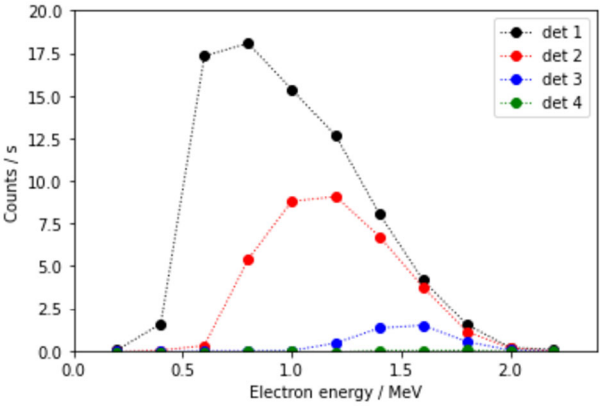


**Fig. 24** Electron energy scans for EDH in EMON facility with $^{90}Sr$ source

PSI secondary beams area PiM1. This allowed for covering energies from 100 keV up to 40 MeV and sampling the whole energy sensitivity range of the EDH. Further tests are planned for the cruise phase.

### 5.5.1 Electron Monochromator EMON

The response curves of the EDH sensors in the EMON monochromator are presented in Fig. 24. The EMON covers energies from 100 keV to 2.1 MeV. The presented data were obtained using settings with no coincidences. The first three channels show non-zero responses to the electrons, while deeper detectors see no electrons. The response value depends on the electron energy. The initial rise of the responses corresponds to opening of deeper channels to electron energy while the decrease is due to the electron source energy spectrum showing lower efficiency after about 1 MeV. The overall sensitivity of the electron detections is lower due to the increased noise and, thus, higher values of the LT discriminator thresholds.

### 5.5.2 High Energy Electrons in PiM1

The test with high-energy electrons at the PSI PiM1 area was done using threshold settings similar to those of EMON. The runs were performed twice using no coincidences and simple double coincidences. The responses are presented in Fig. 25. For no coincidence pattern, they are rather flat, with values similar between all sensors. With applied coincidences, the rate in deeper detectors drops much faster due to accumulated low-efficiency factors. This implies that the initially proposed coincidence scheme should be modified to increase detection efficiency.

## 5.6 Proton Energy Scans

Proton responses were measured using energies between (6) 10 MeV and 200 MeV. All runs were done with constant proton fluxes. The thresholds of all PDH channels were set above the noise (about 180 keV). The measurements were performed at one normal angle only. Two different coincidence modes were used. The first mode had the no-coincidence conditions set, i.e., each diode operated independently. The second mode used a double coincidence pattern. The responses for the coincidence case are shown in Fig. 26.

As one can see, the energy bins show semi-equal spacing in the energy logarithmic scale. While the first five channels exhibit only a small decrease in the response value, the last three channels are much less efficient. Further tests are planned for the cruise phase.

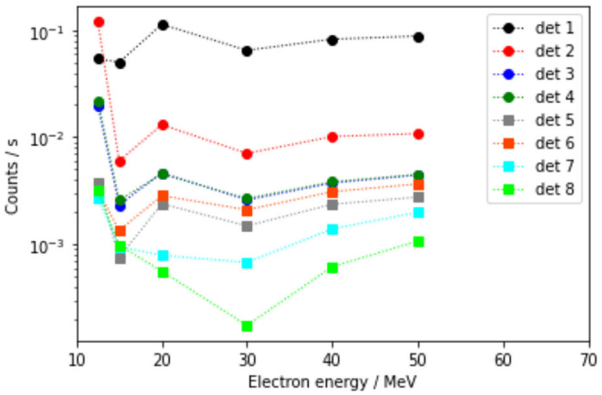


**Fig. 25** High energy electron responses in EDH with coincidence scheme applied for all detector-related energy bins. The initial coincidence scheme was used: coincidence chain of sensors with the last sensor used in anti-coincidence

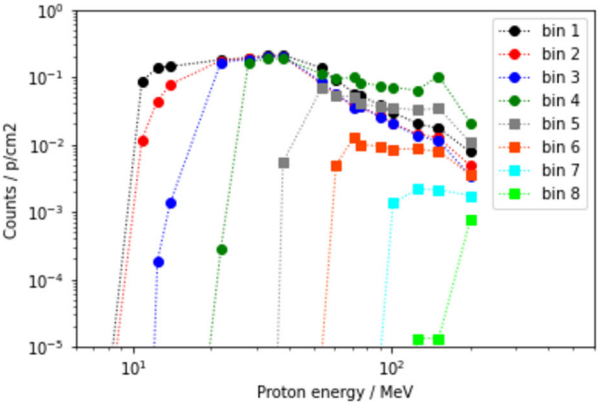


**Fig. 26** Proton energy scans for PDH with coincidence scheme applied for all detector-related energy bins. The initial coincidence scheme was used: coincidence chain of sensors with the last sensor used in anti-coincidence

## 5.7 Dead-Time and Linearity

The response linearity was tested with the 200 MeV protons and variable fluxes for both PDH and EDH subsystems. Any observed deviations of count rate from a linearity as a function of the flux would require additional corrections for instrument dead-time. They would compensate for events lost (ie. not counted) due to instrument insensitivity caused by processing other events. Both RADEM detectors showed very good linearity levels and no need for dead-time corrections. In both cases, the detection rates scale directly with the applied proton fluxes as anticipated based on the ASIC data sheet specifications. The results are presented in Fig. 27 for three preselected channels. The linear fits show the high level of linearity found for each diode with all fit coefficients R=0.99.

## 5.8 Coincidence Scheme

Results based on the effective area measurements and threshold scans revealed lower efficiency for electron detection. It is caused by higher levels of instrument noise. The effect is further magnified in coincidences, especially when adding additional conditions to the coincidence chain. Therefore, a new, optimized pattern of the coincidence matrix is defined for EDH to increase its detection efficiency. In the case of PDH, the settings can remain as originally designed. The required threshold values for proton detection were already set

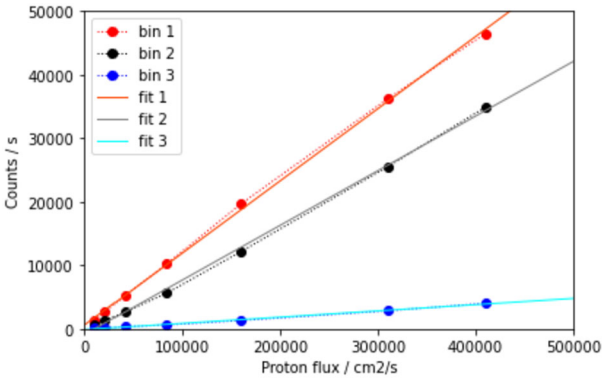


**Fig. 27** Deadtime and linearity test in the PDH

**Table 10** EDH coincidence matrix (1 - coincidence, 0 - anti-coincidence)

| Bin no<br>Threshold | Bin1<br>LT, HT | Bin2<br>LT, HT | Bin3<br>LT, HT | Bin4<br>LT, HT | Bin5<br>LT, HT | Bin6<br>LT, HT | Bin7<br>LT, HT | Bin8<br>LT, HT |
|---|---|---|---|---|---|---|---|---|
| Det1 | 1,0 | 1,0 | -,- | -,- | -,- | -,- | -,- | -,- |
| Det2 | -,- | 1,0 | 1,0 | 1,0 | 1,0 | 1,0 | 1,0 | 1,0 |
| Det3 | -,- | -,- | 1,0 | -,- | -,- | -,- | -,- | -,- |
| Det4 | -,- | -,- | -,- | 1,0 | -,- | -,- | -,- | -,- |
| Det5 | -,- | -,- | -,- | -,- | 1,0 | -,- | -,- | -,- |
| Det6 | -,- | -,- | -,- | -,- | -,- | 1,0 | -,- | -,- |
| Det7 | -,- | -,- | -,- | -,- | -,- | -,- | 1,0 | -,- |
| Det8 | -,- | -,- | -,- | -,- | -,- | -,- | -,- | 1,0 |

**Table 11** PDH coincidence matrix (1 - coincidence, 0 - anti-coincidence)

| Bin no<br>Threshold | Bin1<br>LT, HT | Bin2<br>LT, HT | Bin3<br>LT, HT | Bin4<br>LT, HT | Bin5<br>LT, HT | Bin6<br>LT, HT | Bin7<br>LT, HT | Bin8<br>LT, HT |
|---|---|---|---|---|---|---|---|---|
| Det1 | -,1 | 1,- | 1,- | 1,- | -,- | -,- | -,- | -,- |
| Det2 | 0,- | 1,1 | -,- | -,- | 1,- | 1,0 | -,- | -,- |
| Det3 | -,- | -,- | -,1 | -,- | -,- | -,- | 1,- | 1,- |
| Det4 | -,- | -,- | 0,- | -,1 | -,- | -,- | -,- | -,- |
| Det5 | -,- | -,- | -,- | 0,- | -,1 | -,- | -,- | -,- |
| Det6 | -,- | -,- | -,- | -,- | 0,- | -,1 | -,- | -,- |
| Det7 | -,- | -,- | -,- | -,- | -,- | 0,- | -,1 | -,- |
| Det8 | -,- | -,- | -,- | -,- | -,- | -,- | 0,- | 1,- |

above the noise level found in PDH. The proposed new coincidence schemes for both EDH and PDH are presented in Table 10 and Table 11, respectively. The thresholds proposed for initial settings of all ESD sensors would be LT=150 keV and HT=300 keV. These values in space should be verified and tuned for the noise levels. For the PSD the values of LT are proposed to be kept at 300 keV and the HT set at for D1:2000 keV, D2-D4:1000 keV, D5-

**Table 12** Fulfilment of RADEM requirements for the JUICE mission

| No | Requirement | Status | Results | Remark |
|---|---|---|---|---|
| 1 | Electron energy range 0.3 - 40 MeV | Tested | passed | - |
| 2 | Max. detectable electron flux $10^9$ /cm2/s | Tested | passed | - |
| 3 | Proton energy range 5 - 250 MeV | Tested | passed | - |
| 4 | Max. detectable proton flux $10^8$ /cm2/s | Tested | passed | - |
| 5 | Eight bins space equally on log energy scale | Tested | passed | - |
| 6 | Separation of electrons and protons | Tested | passed | - |
| 7 | Detectable ion species Helium - Oxygen | BB use | passed | indirect test with Iron |
| 8 | Ion LET range 0.1-10.0 MeV cm $mg^{-1}$ | BB use | passed | indirect test with Iron |

D6:700 keV and D7-D8:500 keV. The same space verification scheme should be applied. One can also retune the PSD for detection of protons using LT and heavy ions with HT.

### 5.9 Performance

The RADEM performance during calibration confirmed that all requirements for operation onboard the JUICE mission were fulfilled. The summary is presented in Table 12. The most important result from the calibrations was the higher detector noise and, consequently, the lower detection efficiency, especially for electrons in the EDH. No other major issues concerning the requirements were found. The electron detection efficiency can be improved with the newly proposed coincidence matrix for EDH. The higher noise levels in DDH reduce its dynamic range for electron directionality measurements even further. Its proton detection capability corresponds to original expectations. Performance of the PDH meets the expectations from the requirements despite higher values of the noise. It is due to the fact that even such noise levels do not influence proton detection efficiency.

## 6 Operation in Space

### 6.1 Commissioning

The Near Earth Commissioning Phase of RADEM started directly after the completion of the JUICE Low Earth Operation Phase LEOP in April 2023. It was split into the instrument operational performance (IOP) and the radiation monitoring performance (RMP). During the IOP phase, the instrument was tested based on a set of telecommands and detections of the corresponding telemetry. This phase specifically verified the RADEM health status. During the RMP phase, we validated RADEM performance for detecting energetic particles. Once the radiation monitoring performance is tested and compared with the requirements, the results can be used to optimize settings and operation parameters. Table 13 shows the steps of RADEM commissioning.

After switching RADEM on, the received housekeeping telemetry data packets were verified. All essential parameters, such as voltages, currents, and temperatures, behaved as anticipated. No malfunctioning was observed after comparison of other housekeeping parameters with their nominal values. The housekeeping data were closely monitored during the whole commissioning period that started subsequently. The first RDM-01 test aimed to

**Table 13** Steps of RADEM commissioning

| Procedure | Description |
|---|---|
| RDM-01 | Instrument ON/OFF and Health Status Check |
| RDM-02 | Detector Noise Scan |
| RDM-03 | Internal ASIC pulse generator tests of RADEM channels |
| RDM-04 | Detection of Cosmic Rays in Single Mode |
| RDM-05 | Cosmic rays test of Coincidence Schemes |

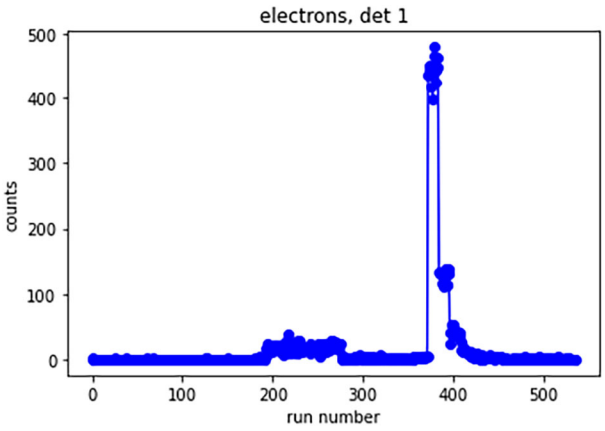


**Fig. 28** Noise scan example for the EDH Detector D1 performed with the LT discriminator

verify RADEM switching on and off and the status of the HK file. No errors were detected. Power consumption was around 3.3 W, as anticipated.

The second test, i.e., RDM-02 Detector Noise Scan, was done with all detectors switched on with the HV set to nominal values, and a single detector logic configuration was applied. During this test the LT and HT threshold scans were performed for each detector using predefined steps around the nominal threshold value. Each settings was applied and measurements were performed ten times with each measurement taken as a separate run. These tests were equivalent to threshold scans with done proton beams on-ground. In space protons were replaced by Cosmic Rays. The results showed that all detector channels except of one in the HIDH behaved as expected. The malfunctioning HIDH channel did not show any counts. An example of threshold scans is shown in Fig. 28. Different values of the counts collected during data-taking runs correspond to varying levels of the LT discriminator.

The next test, RDM-03, used the ASIC pulse generator to verify the detector's threshold sensitivity to internal pulses sent by RADEM electronics.

Results in Fig. 29 are presented for the PDH Detector D4 and exhibit clear steps related to changing pulse amplitudes. The internal pulser can be used to check single-channel functionality such as counting efficiency and threshold stability. A calibration of the pulse amplitudes with the Cosmic Rays is planned for further stages of the mission.

The first RDM-04 tests with Cosmic Rays detection verified single detector functionality. We executed threshold scans using long runs to collect sufficient data. An example for the EDH Detector 1 is shown in Fig. 30. The LT threshold values were increased with the run number resulting with decreasing number of counts from Cosmic Rays. Such tests will be used in the future for periodic in-flight calibrations and checking threshold stability.

The final test, RDM-05, was similar to the previous one. It used Cosmic Rays for detection with a coincidence scheme applied. RADEM was set to measure particles coming

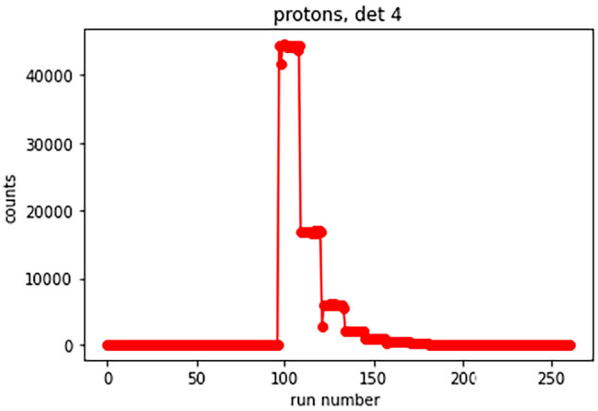


**Fig. 29** Pulser scan example for the PDH Detector D4 done using various pulser amplitudes

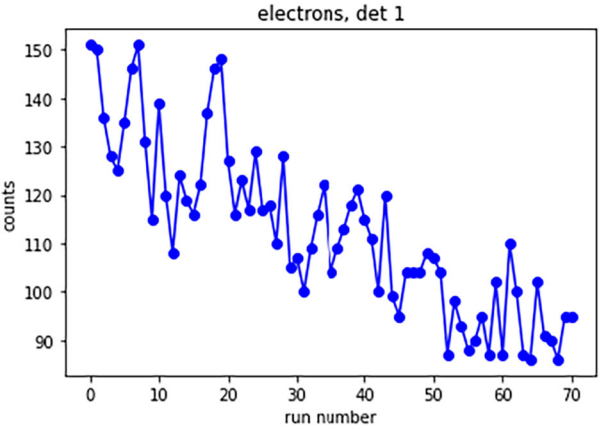


**Fig. 30** Cosmic ray scan in EDH Detector D1 realized with various levels of the LT discriminator

through the entrance collimator. The data, as expected, had a much lower number of counts than the case of no coincidences.

The results from the commissioning showed the proper operation of RADEM. Only in the HIDH is one sensor not working as expected, but the second one shows good responses. Further optimization of the RADEM settings, i.e., threshold values and coincidence matrices, will be performed during its in-flight calibration and optimization checks during the cruise phase.

## 6.2 Cruise Phase Settings

During the cruise phase, RADEM is fully operational, continuously measuring the radiation environment in interplanetary space. In particular, the inner solar system between the orbits of Venus and Mars i.e. approximately 0.70 - 1.66 au (1 astronomical unit (au) - $150{\cdot}10^6$ km) will be mapped over three years, and the rest of the time, the spacecraft will move into the outer solar system, covering the distance between Mars and Jupiter (1.66-5.0 au). The spacecraft's orientation in space will be set according to the JUICE trajectory needs. Thus, the RADEM field of view will have a different point of view with respect to incoming solar particles, depending on the phase of the mission. Galactic Cosmic Rays and occasional Solar Energetic Particle events will dominate the radiation environment during the cruise phase.

**Table 14** EDH coincidence matrix proposed for the cruise phase (1 - coincidence, 0 - anti-coincidence)

| Bin No<br>Threshold | Bin1<br>LT, HT | Bin2<br>LT, HT | Bin3<br>LT, HT | Bin4<br>LT, HT | Bin5<br>LT, HT | Bin6<br>LT, HT | Bin7<br>LT, HT | Bin8<br>LT, HT |
|---|---|---|---|---|---|---|---|---|
| Det1 | 1,0 | 1,0 | -,- | -,- | -,- | -,- | -,- | -,- |
| Det2 | -,- | 1,0 | 1,0 | 1,0 | 1,0 | 1,0 | 0,- | 0,- |
| Det3 | -,- | -,- | 1,0 | -,- | -,- | -,- | -,- | -,- |
| Det4 | -,- | -,- | -,- | 1,0 | -,- | -,- | -,- | -,- |
| Det5 | -,- | -,- | -,- | -,- | 1,0 | -,- | -,- | -,- |
| Det6 | -,- | -,- | -,- | -,- | -,- | 1,0 | -,- | -,- |
| Det7 | -,- | -,- | -,- | -,- | -,- | -,- | 1,0 | -,- |
| Det8 | -,- | -,- | -,- | -,- | -,- | -,- | -,- | -,1 |

Although the instrument will measure solar particles independently of the pointing direction of the spacecraft, accurate spectroscopy of such events is possible for cases where the average direction of incoming particles is aligned with the RADEM field of view. The side shielding of its telescopes restricts the minimum penetrating energies to more than 65 MeV for protons and about 6 MeV for electrons. Therefore, the settings of the RADEM proton telescope will be similar to the nominal mode settings used during the Jupiter operation phase. The electron telescope settings may differ from the nominal Jupiter phase for its two last sensors. They will work in a single detection mode with thresholds optimized for Galactic Cosmic Ray detection. This way, they will be sensitive to the passage of solar transient events, such as Coronal Mass Ejections, which are known to produce a sudden steep depression in the intensity of Galactic Cosmic Ray fluxes. These decreases are known as Forbush decreases and have been observed even well beyond Jupiter's orbit (e.g. Witasse et al. 2017). The heavy ion sensor settings will be tuned to detect carbon and heavier ions, similar to the Jupiter exploration phase. Also, the directionality sensor settings will be similar to those in the Jupiter exploration phase. Such settings will be very useful during special periods of the cruise phase, including moon and planet approaches during gravitational assists or pointing campaigns during which one can detect Jovian electrons. The proposed RADEM settings for the cruise phase are using threshold values determined during in-flight calibrations finished before LEGA in August 2024. The proton coincidence matrix is defined in Table 11. The electron coincidence matrix is defined in Table 14. The last two channels are optimized for the detection of electrons and protons coming through the shielding.

### 6.3 Settings for Jovian Phase

The Jovian phase settings are nominal for RADEM operation. They allow for spectroscopic measurements of electrons and protons coming through the entrance windows. They are also optimized for electron/proton separation and suppression of the background from particles penetrating through the shielding. The coincidence matrices applied for such settings used the logic and thresholds tuned to maximize detection efficiency and spectroscopic accuracy. Fine-tuning in the Jovian environment will include adjustments according to the different particles' absolute and relative radiation levels. The threshold values will be set after the last in-flight calibration before reaching the Jupiter system. The proposed RADEM coincidence matrices are defined based on the calibrations - see Table 10 and Table 11.

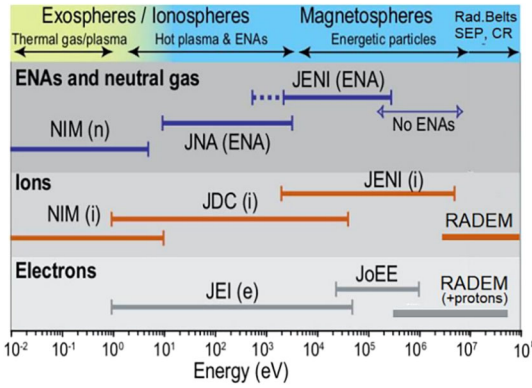


**Fig. 31** Energy ranges of RADEM and of the six instruments (NIM, JNA, JENI, JDC, JEI, and JoEE) of the Particle Environment Package. Figure adapted from Hussmann et al. (2014)

### 6.4 Calibrations in Space

Calibrations of RADEM will be performed in regular annual intervals to verify the monitor's settings and validate its response functions needed for unfolding particle fluxes and energy spectra. During the cruise phase, the Galactic Cosmic Rays will be routinely used for this purpose based on single-diode detections. RADEM will be configured for a non-coincidence mode and threshold scans. The duration of each scan will be long enough to collect a statistically sufficient number of events. Fine corrections aimed to increase the calibration accuracy will be applied based on the Cosmic Rays transmission through the JUICE spacecraft modeled with the GEANT4 simulation code. One should be aware that this calibration procedure won't be enough for the Jovian phase. Therefore, apart from the Cosmic Rays scans, additional tests with the RADEM internal pulser will be performed using predefined pulser amplitudes and the same threshold settings as for the Cosmic Rays calibrations. This calibration method will be applied for RADEM during its Jovian phase, anticipating that very high levels of particle fluxes from the Jupiter radiation belts will make it difficult to use the cosmic Rays only.

### 6.5 Cross-Calibrations

In addition to the calibration methods described above, RADEM measurements will be compared to observations provided by other instruments onboard JUICE. Two such instruments belong to the Particle Environmental Package (PEP) suite (Barabash et al. 2025, this collection) for which RADEM provides high energy extensions. One of them is the Jovian Energetic Electrons (JoEE) instrument, which has an overlapping energy range with RADEM from 300 keV up to 1 MeV and provides a sufficiently broad range for cross-calibrations (see Fig. 31). The second one is the PEP Jovian Energetic Neutrals and Ions (JENI) instrument, for which the overlap covers the first proton energy bin of RADEM starting at 5 MeV. The first comparisons is made during the Lunar-Earth gravitational assist in August 2024, during which the JUICE is passing through the Van Allen radiation belts. As the spacecraft crosses both the proton and electron belt, cross-calibrations are possible for both RADEM telescopes, with the PEP instruments taking precautions for different pointing directions and field-of-view. The belt crossing also allows the instrument to be tested under high and directional fluxes of particles in anticipation of the even more intense radiation at Jupiter. these measurements are currently under evaluation. Additional checks and comparisons will be made during the cruise phase using observations from other radiation monitors sensitive to

particle energies similar to RADEM. Among others, it includes BERM on BepiColombo (Pinto et al. 2017), Energetic Particle Telescope EPT and High Energy Telescope HET onboard of Solar Orbiter, or several other monitors such as IREM on Integral (Hajdas et al. 2003) and RMUs on Sentinel and Meteo-satellites, conducting measurements in parallel to RADEM. The detector systems of these monitors are different from RADEM. They also fly onboard missions separated from JUICE by very large distances. Thus, any comparison of observations must be performed with special care, and differences in their field of view, dynamics of particle propagation in interplanetary space, or orientation with respect to the magnetic field must be considered.

## 7 Science Overview

RADEM has two broad objectives within the JUICE mission: On one hand, RADEM serves as a radiation monitor observing its most dangerous energy regime in terms of radiation damage. It ascertains safety levels of the spacecraft and its scientific payload, giving also the context for data analysis of other science instruments onboard JUICE affected by radiation.[3] The most relevant other scientific instruments are PEP (Barabash et al. 2025, this collection), J-MAG (Dougherty et al. 2025, this collection), and RPWI (Wahlund et al. 2025, this collection) for cross-calibration and identification of radiation-induced background in these plasma instruments. On the other hand, RADEM serves as an instrument that will contribute to the scientific investigations of JUICE both during the cruise phase (Sect. 7.1) and in the Jovian and Ganymede magnetospheres (see Sect. 7.2). In the last subsection of this chapter (Sect. 7.3), early science data from the beginning of the cruise phase are shown.

### 7.1 Science Goals for Cruise Phase

RADEM offers the unique chance to measure high-energy particle environments from Venus to Jupiter continuously. During the cruise phase, RADEM data will be used for several different science objectives involving aspects of (1) In-flight calibration and optimization, (2) monitoring of Solar Energetic Particles, Galactic Cosmic Rays, and their variability, (3) measuring and tracking solar energetic events, (4) detecting and characterizing escaping relativistic Jovian electrons and, (5) monitoring planetary environments (Venus, Earth, Jupiter). We elaborate on some of these aspects below:

- In addition to using its internal pulser circuit, the RADEM in-flight response must be characterized in regular intervals using ambient Galactic Cosmic Rays (GCRs). GCRs have the best-defined and the least variable energy spectrum compared to the various populations RADEM is designed to measure and thus serve as the optimal calibration target. In addition, several spacecraft and platforms provide precision GRC spectra at 1 AU, where RADEM will take measurements for several years (Roussos et al. 2020). The Earth's magnetosphere radiation environment, which will be sampled during the three Earth flybys of JUICE, is also an excellent calibration target for RADEM. While Earth's magnetosphere is variable, it is monitored by many spacecraft with energetic particle instrumentation that will obtain simultaneous observations and key context for RADEM. Furthermore, Earth's inner proton radiation belts, the most steady component of Earth's magnetosphere, is a similarly excellent calibration target for RADEM, similar to GCRs (Selesnick and Albert 2019). This aforementioned procedure validates and optimizes its original parameter

[3] see Sect. 5.2.1 in the JUICE Definition Study Report (Hussmann et al. 2014).

settings based on ground calibration data and the modeling of responses. Such optimization is crucial for all other science objectives and interpreting data from other science instruments acquired later during the Jupiter orbit phase or the arrival to Jupiter (escaping Jovian electrons - see below). The verified and optimized settings for the cruise phase will differ from the parameter settings in Jupiter's magnetosphere, so further optimizations may be necessary once JUICE enters Jupiter's magnetosphere. When the other science instruments on JUICE are active, the RADEM observations can be correlated with magnetic field measurements by J-MAG (Dougherty et al. 2025) and other simultaneous observations. The RADEM data will also be compared with older observations, e.g., by SREM instruments onboard the Planck and Herschel missions at L2 or still ongoing IREM observations on the Integral satellite along its GTO-like orbit (Kuulkers et al. 2021).

- A direct trajectory of a potential manned flight from Earth to Mars would take roughly 250 days (Zeitlin et al. 2013). In contrast, the cruise time spent by JUICE between Earth, Venus, and Mars orbit is six years because of several gravity assists. This prolonged duration will provide more detailed coverage and better statistics of the variability of the radiation environment between Earth and Mars, covering more than half a solar cycle. This is crucial to better understanding the solar activity and the propagation mechanisms of solar particles in the interplanetary space, considering solar wind conditions and current solar mass ejection fields on the path of Coronal Mass Ejections. So far, the most accurate data for the absorbed dose values come from the RAD instrument onboard the MSL mission (Zeitlin et al. 2013; Matthiä et al. 2017). The authors found that about 90% of the dose originated from Cosmic Rays during relatively quiet solar conditions. These values were already very high, reaching on average about 1.84 mSv/day (0.18 rad/day) or 0.5 Sv for the whole cruise phase. However, strong SEP events can provide comparable dose values in just a few days and thus increase the stochastic SEP dose fraction incurred during a future manned mission to Mars by a very large factor (Odenwald et al. 2006).
- GCRs are highly energetic protons and heavier ions entering our solar system from galactic and extra-galactic sources at almost light speed (energies $> 1$ GeV). Studying GCRs with RADEM during the cruise phase is also interesting because their modulation informs us about the interaction of the heliosphere with the surrounding medium and loss processes inside the solar system (see, e.g., Potgieter 2017 and references therein, Dialynas et al. 2022; Giacalone et al. 2022 and Hill et al. 2020). The spectral and intensity maps as a function of distance from the Sun and with Solar Wind parameters will allow for a better understanding of the interaction between Cosmic Rays and the heliosphere during the 8-year cruise phase. In particular, RADEM will precisely measure GCR fluxes at the low-energy part of their energy spectra, which is subject to the strongest solar modulation. It can inform GCR transport models by measuring the GCR radial intensity gradient across the JUICE interplanetary trajectory. Gradient calculations can be performed with standalone RADEM measurements or by combining RADEM with reference simultaneous GRC measurements at 1 AU (Roussos et al. 2020; Honig et al. 2019) or at the innermost solar system by BepiColombo and Solar Orbiter (for a first example, see Fig. 37). RADEM will be able to detect both proton and electron spectra and thus improve our knowledge of the interaction between GCR and solar activity (e.g., Forbush decreases) and their impacts on the space environment of the inner solar system.
- With a default measurement frequency of 60 s, the RADEM will provide time-resolved spectroscopy of the radiation environment along the JUICE trajectory for electrons, protons, and heavy ions. The Cosmic Rays, with their slow variability, will be easily distinguishable from more dynamic solar events. Monitoring these events will contribute to the energy spectra of the above particle species and extend to the Forbush decrease measurements (e.g., Raghav et al. 2017). Further correlations with either electrons above 300 keV

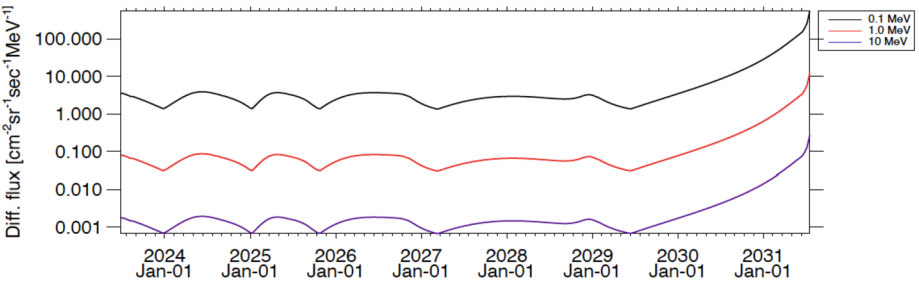


**Fig. 32** Predicted Jovian electron fluxes along the JUICE interplanetary trajectory, based on a Jovian electron source model by Vogt et al. (2018), a propagation model as in Conlon (1978), transport coefficients in del Peral et al. (2003), and a solar wind velocity of 400 km/s. Predictions are for the quiet time Jovian electron fluxes. Estimates are based on a model developed for the ESA project FIRESPELL (see acknowledgements)

measured with EDH or protons above 5 MeV measured with PDH will also be possible, and the DD will provide accurate information on their angular anisotropies. This will improve our understanding of the dynamics and propagation of Solar Energetic Particle Events and Coronal Mass Ejections across the Solar System.

- Jupiter is a well-established source of energetic electrons (∼100 keV – ∼30 MeV) in the heliosphere, with the corresponding fluxes dominating in this energy over the quiet-time solar electron spectra and that of GCR electrons within about 10 AU (Strauss et al. 2011; Vogt et al. 2018). Because Jupiter is a well-located point electron source, observations of the Jovian electrons away from Jupiter are important for evaluating particle transport processes across the heliosphere. Far from Jupiter and around 1 AU, Jovian electrons should manifest in RADEM electron measurements as a weak signal with an approximate 10-14 month periodicity, the synodic period between JUICE and Jupiter (Strauss et al. 2024). On approach to the planet, JUICE is in an ideal position to monitor Jovian electrons as it approaches Jupiter approximately aligned with the Parker spiral connecting JUICE to Jupiter's magnetosphere, along which Jovian electrons are primarily propagating. At the same time, RADEM will also be monitoring how Jovian electron spectra change in response to variable solar wind conditions. Jovian electron fluxes are expected to gradually increase by about 2 orders of magnitude between 2029 and the Jupiter orbit insertion (Fig. 32). In this phase, Jovian electron bursts (episodic enhancements of Jovian electron escape) and intervals with periodicities in the Jovian electron spectra (Krupp et al. 1999; Vogt et al. 2018) are expected to increase in frequency.

### 7.2 Science Goals for the Jovian System

Jupiter's huge magnetosphere offers the most extreme particle radiation environment in our solar system outside the environment in close vicinity of the Sun itself (Roussos et al. 2022). Jupiter's magnetosphere is home both to thermal plasma and suprathermal (soft energetic partilces) co-rotating with the magnetic field of Jupiter (eV to ∼ 10 keV energies) and to more energetic particle radiation, possibly reaching GeV energies for some species (Kivelson et al. 2004; Khurana et al. 2004; Bagenal et al. 2016; Roussos et al. 2022). Characterizing this environment is indispensable to understanding Jupiter itself and the radiation environment of the Galilean moons inside this magnetosphere. The latter must be achieved if we are to distinguish exogenic from endogenic contributions to the physical and the chemical properties of the exospheres and on the surfaces of these bodies. Therefore, past, active,

and future missions to study Jupiter and its moons are equipped with plasma instruments and radiation monitors. Previous and ongoing observations with Galileo (Krupp et al. 2023) and Juno (Enghoff et al. 2024) demonstrated the scientific value of high-energy particle measurements in the Jovian magnetosphere, highlighting the prospects for a dedicated, high-energy particle instrument (combined with a plasma instrument suite and other in-situ instruments) that will be continuously operating inside the Jovian magnetosphere for several years.

Measuring the energetic particle populations is crucial to obtain an accurate take on the space environment of Jupiter and its influence on the Jovian moons and allows us to study creation and acceleration processes for charged particles (i.e., the importance of magnetic reconnection, the way co-rotation breaks down at larger Jovian distances Bolton et al. 2015) and how Jovian's magnetosphere filtrates external energetic particles from the solar wind and heliospheric (e.g. Anomalous Cosmic Rays) and galactic sources (Cosmic Rays).

The science goals for RADEM in the Jovian system can be organized into three groups: (1)Mapping the particle radiation environment of the Jovian magnetosphere, (2) evaluating the access of GCRs and SEPs penetrating the Jovian magnetosphere, and (3) mapping the local magnetospheric interaction environments of Europa, Ganymede, and Callisto at high particle energies. Specifically:

- RADEM is ideally placed to advance the quality of high energy particle radiation maps of Jupiter's magnetosphere. The trajectory of JUICE, combined with the continuous operations of RADEM, means that the statistical sampling of Jupiter's radiation environment will substantially improve, particularly for low and mid-latitudes and for magnetospheric regions inside the orbit of Callisto. The sampling time for energetic particle spectra near the magnetic equator will range from a minimum of 2-3 days per broad, 6 h-wide local time sector (noon, midnight, dawn, dusk), up to a maximum of 1-1.5 weeks (see JUICE Working Group 3/Magnetospheric Science paper, this journal). In comparison, radiation belt coverage from Galileo's discontinuous measurements barely exceeded a few hours (Yuan et al. 2021) for a local time sector and L-shell, whereas Juno, due to its high inclination, long-period, and precessing orbits, does not sample the low latitude magnetosphere more than few times at a given L-shell/local time pair. In addition, thanks to short-period orbits that offer a near-continuous residence of JUICE in the vicinity of the Galilean moons, revisit times of similar magnetospheric regions will be substantially reduced compared to earlier missions. This means that shorter variability scales can be captured in the radiation belts compared to Juno and Galileo ($>1$ month orbital periods). This will be particularly important for resolving magnetospheric transients and their evolution, their associated acceleration mechanisms, and for disentangling temporal from spatial variability patterns (Yuan et al. 2021, 2024; Roussos et al. 2018b; Hao et al. 2020).
- For mildly relativistic electrons of several hundred keV, the 28 angular sectors of RADEM-DD will greatly complement the pitch angle coverage of the PEP/JoEE instrument, which uses three out of its nine view directions for 0.3-1 MeV electron measurements (Fig. 33). For the MeV energy range, instantaneous pitch angle coverage from the unidirectional PDH, EDH and HIDH units is not achievable, still, pitch angle distributions can be obtained over the time scale of regular JUICE slews, and statistically over the three yearlong Jupiter magnetosphere tour. Figure 34) that the RADEM unidirectional units will achieve a total sampling time ranging between 0.5-6.5 days per 10 deg of pitch angle, for any given L-shell (McIlwain L-parameter) from L=9 to L=50). Such extensive pitch angle coverage for MeV electrons and ions outside Europa's orbit will be achieved for the first time. Previous observations by Galileo have achieved that only few selected locations or time periods, particularly around moon flybys (Nenon et al. 2022; Krupp et al. 2023). Resolving the shape of pitch angle distributions as a function of L-shell would be

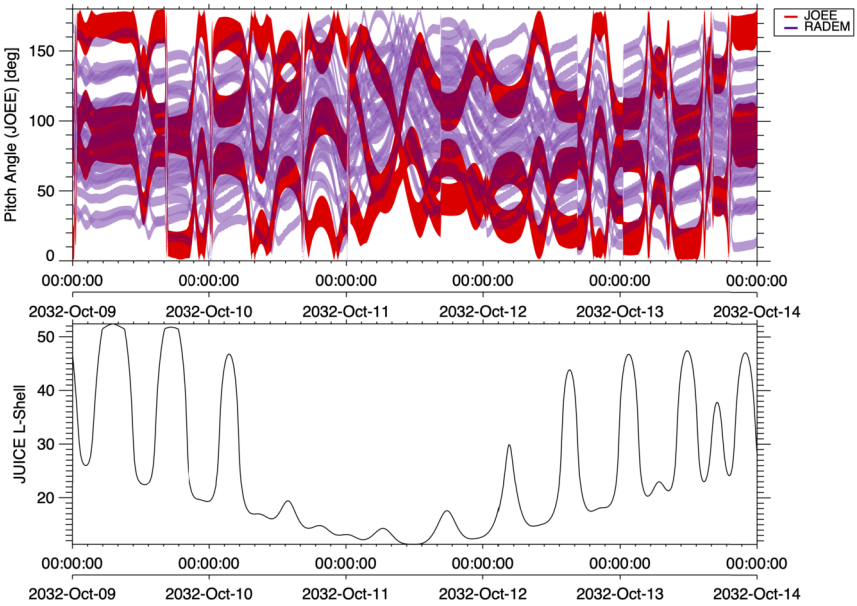


**Fig. 33** Combined pitch angle coverage of RADEM's directionality detector (blue shading) and PEP/JoEE (red shading) for a typical JUICE perijove inward of Ganymede's orbit. Pitch angle coverage and the corresponding L-shell position of JUICE were calculated using the JUICE NAIF/SPICE kernels and a Jovian magnetospheric field model (Wilson et al. 2023). Each coverage stripe corresponds to a single RADEM DD or PEP/JoEE detector pixel. Variations in the pointing of each pixel are due to the rotation of the Jovian magnetic field and/or simulated JUICE re-orientations

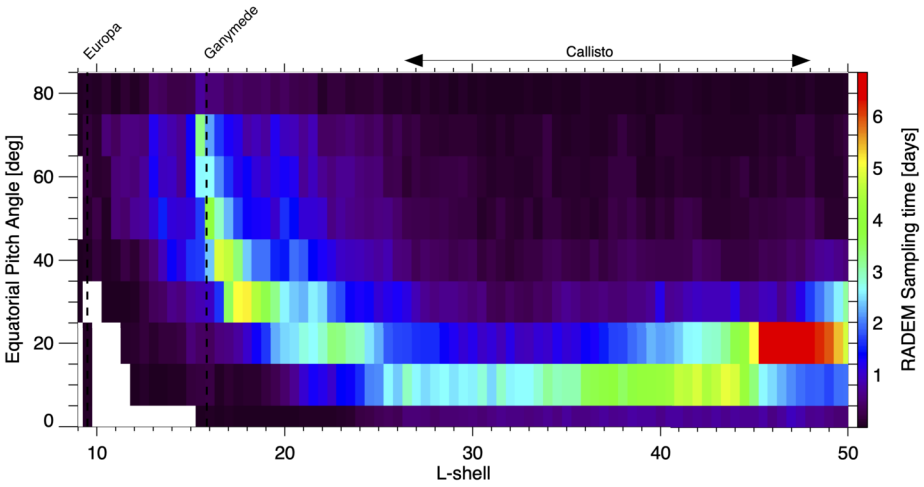


**Fig. 34** Expected equatorial pitch angle coverage by RADEM's unidirectional detector heads (EDH, PDH, HIDH) for the MeV electron and ion energy range, over the whole Jovian magnetosphere tour of JUICE. The equatorial pitch angle corresponds to the pitch angle that same particle would have, if RADEM would observe it at the magnetic equator. Pitch angle pointing and the corresponding L-shell position of JUICE were calculated using the JUICE NAIF/SPICE kernels and a Jovian magnetospheric field model (Wilson et al. 2023). As Callisto is located deep in the Jovian current sheet, its magnetically mapped location extends over 20 L-shells

key for evaluating source, acceleration, transport and loss processes of energetic particles (Tomás et al. 2004; Kollmann et al. 2016; Ma et al. 2021; Liu et al. 2021; Clark et al. 2018).

- Thanks to its energy coverage and channel design alone, RADEM will peek into unexplored regimes of the Jovian magnetosphere, particularly for the relativistic electrons and penetrating >10 MeV protons. Even though spectroscopy of penetrating relativistic MeV electrons is challenging, RADEM-EDH comprises eight different electron integral channels with starting energies between 1 and 40 MeV that will substantially improve the fidelity of spectral inversions and thus better establish the presence of spectral peaks or breaks that can be revealing of processes like acceleration by waves or coherent plasma flows (Hao et al. 2020; Roussos et al. 2022). For comparison, Galileo-based electron spectra in the MeV range are based on just two integral channels, with the highest energy one starting at about 11 MeV (Kollmann et al. 2018). Similarly, published proton measurements above about 10 MeV are almost non-existent at Jupiter and beyond the orbit of Europa (Nénon et al. 2018, and references therein). These measurements may particularly help detect new components of Jupiter's radiation belts that have a GCR origin (e.g., Cosmic Ray Albedo Neutron Decay / CRAND proton belts Selesnick and Albert 2019; Roussos et al. 2022) or solar origin, e.g. transient radiation belts associated to the entry of solar energetic protons, as observed at Saturn (Roussos et al. 2018a). Such measurements can be complemented by RADEM-HIDH heavy ion observations, which can sufficiently separate energetic carbon (heliospheric origin) from oxygen and sulfur (magnetospheric origin) (Cohen et al. 2001). The access and the trapping efficiency of high energy protons and heavy ions in magnetodisk-shaped magnetospheres can also inform models of radiation belt ion transport, CRAND generation, and the ion irradiation of the Jovian atmosphere and moon surfaces (Selesnick et al. 2001; Selesnick 2002; Nordheim et al. 2019; Enghoff et al. 2024).
- A by-product RADEM's mapping of the Jovian particle radiation environment (see point [a]), will be that these maps will also include the ambient energetic particle spectra with which the icy Galilean moons interact with. The properties and the variability time scales of these spectra are key for evaluating the structure and state of various components of a moon magnetosphere interaction, such as the structure of an exosphere (Plainaki et al. 2018; Vorburger et al. 2019; Galli et al. 2022; Vorburger et al. 2024). In addition, it may inform interpretation of remote sensing spectroscopy observation of icy surfaces, where the production of oxidants depends on the background electron and ion flux (Trumbo et al. 2019; Addison et al. 2023, and references therein). In addition, the presence of the moons and their direct or indirect impact on the Jovian magnetosphere will also be evaluated, such as through the detection by RADEM of distant moon wakes (micro signatures) (Roussos et al. 2013; Herceg et al. 2022) and radiation losses on the moon-originating neutral gas in extended Europa and Io tori (Kollmann et al. 2016; Galli et al. 2022). Callisto's energetic particle interaction observations by Galileo contain many mysteries, including the lack of a clear wake signature, the possible presence of electron beams (Liuzzo et al. 2024; Krupp et al. 2023), that can be studied in more detail thanks to the observations that RADEM, in combination with PEP, will collect over 20 flybys across a very broad regime of particle species, energies, and pitch angles. A significant breakthrough is expected from RADEM's observations while JUICE is in orbit around Ganymede. These will be the first continuous and detailed observations of a planetary moon continuously interacting with high fluxes of suprathermal and relativistic particles, an interaction that may saturate processes involving exosphere formation, chemical and physical surface alterations by particle radiation, and surface charging (Halekas et al. 2005; Nordheim et al.

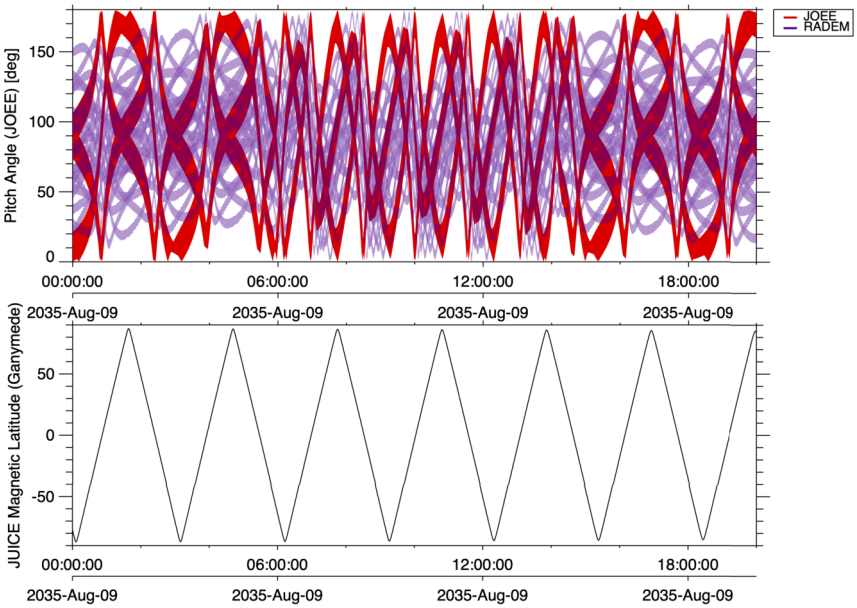


**Fig. 35** Combined pitch angle coverage of RADEM's directionality detector (blue shading) and PEP/JoEE (red shading) for a 1-day period of JUICE in its 500-km altitude orbit around Ganymede. Pitch angle coverage and the corresponding magnetic latitude position of JUICE around Ganymede were calculated using the JUICE NAIF/SPICE kernels, a magnetospheric field model adding the contributions of Jupiter (Wilson et al. 2023), a Ganymede dipole field and induction from a subsurface ocean. Each coverage stripe corresponds to a single RADEM DD or PEP/JoEE detector pixel. Variations in the pointing of each pixel are due to the rotation of the Jovian magnetic field, the simulated JUICE nadir-pointing attitude, and the variation of the JUICE position around Ganymede over its three-hour 500 km orbit

2019; Trumbo 2021). Such conditions at the Earth's moon occur only transiently, during solar energetic particle events. In addition, the internal magnetic field of Ganymede allows for studies on the stability of radiation belt systems in mini-magnetospheres and allows for electron reflectometry measurements, among others (Williams et al. 1997a,b; Williams 2001). Besides the extensive energy and species coverage, the RADEM pitch angle coverage at Ganymede, in combination with measurements by PEP, make all the aforementioned science investigations feasible (Fig. 35).

### 7.3 First Science Data from Cruise Phase

After commissioning in May 2023, RADEM was switched on again on August 31, 2023 in preliminary cruise phase settings, more specifically, in non-coincidence mode at 60 s time resolution and with maximum sensitivity for Cosmic Ray detection. Since that day, RADEM has been continuously measuring science data. In Fig. 36 we show as an example the raw count rates versus time registered in Proton channel 1 over February 2024. These count rates represent particles around 5 MeV initial energy, but because of the non-coincidence mode, both protons entering through the collimator (with energies above 5 MeV) and penetrating through the shielding (with energies above 60 MeV) were registered. The almost constant baseline (median = 5 counts per 60 s) is mostly produced by Cosmic Rays showing stable, temperature independent level of hits; the internal instrument background count rate is orders of magnitude lower. In addition to that baseline, a huge increase in energetic particles

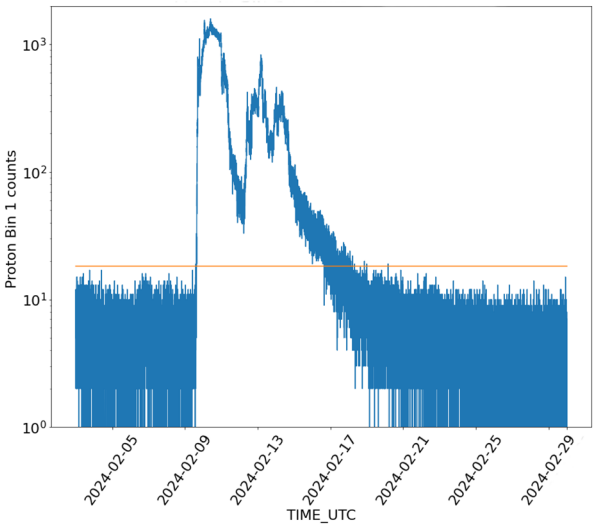


**Fig. 36** Raw count rates (in 60 sec time bins) measured with RADEM proton channel 1 (corresponding to roughly 5 MeV energy) in cruise phase during Feb 2024. The increase in counts starting on Feb 9th was likely caused by a solar flare. The orange line, derived from the GCR background level during quiet times, indicates the 5-$\sigma$ threshold to identify solar events

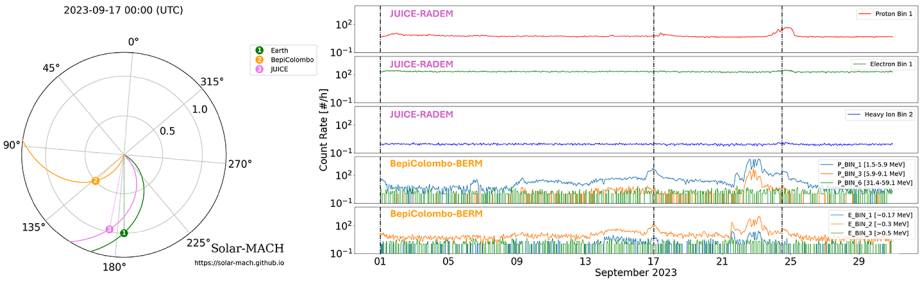


**Fig. 37** Solar Energetic Particle event observed in September 2023 first by BERM on BepiColombo (bottom panel) and then by RADEM on JUICE on 24.&25.9. (top panel showing bin 1 for proton, electron and heavy ion channels). Figure taken from Hajdas et al. (2023), the Solar-MACH plots on the left were generated with the tool provided by Gieseler et al. (2023)

starting on the 9th of February can be seen indicating its possible correlation with a strong Solar Flare released the same day on the Sun (CCMC 2024).

Another example of a Solar Energetic Particle Event registered by RADEM in September 2023 was also observed by other radiation monitors in the inner solar system such as BERM (Pinto et al. 2017) on BepiColombo (see Fig. 37).

## 8 RADEM Archive

The following PDS4[4] RADEM data products will be available in the ESA Planetary Science Archive (PSA) according to the JUICE Science Data Generation, Validation and Archiving Plan (Witasse et al. 2023):

[4]Planetary Data System version 4 (PDS4) is a standard format used primarily by NASA to store and distribute solar, lunar and planetary imagery data.

1. Raw Data - Telemetry packets from all JUICE instruments systematically converted into PDS4 raw data products (uncalibrated) by the Science Ground Segment (SGS). These are raw files both for the housekeeping and for the science data. The former contains instrument variables that are not yet calibrated in their physical units, which is essential to understanding the health and well-functioning of the instrument. The latter contains count rates with a 60-second resolution for all channels in the four RADEM detector subsystems.
2. Calibrated Data - Electron and protons fluxes in physical units (particles/$cm^2$ sr s) and Heavy-Ion Linear Energy Transfer for species from Helium to Oxygen in physical units (MeV $cm^2$ $mg^{-1}$).
3. Derived data - Electron differential energy fluxes. Integral fluxes with angular dependency. Proton differential energy flux (with angular dependency). Total ionizing dose derived from electron and proton differential fluxes.
4. Calibration data - RADEM response functions with derived geometric factors for each detector subsystem. Any other on-ground calibration measurements.
5. Browse products - Small thumbnails with links associated to the science and housekeeping data products from raw to calibrated.
6. Documents - All documents related to the bundle necessary for data use and interpretation.
7. Spice Kernels - The Instrument Kernel (ik) serving as a repository for RADEM-specific geometry and other useful information. It also includes information on RADEM's subsystems FOVs.

## 9 Summary and Conclusions

The Radiation Hard Electron Monitor RADEM is a compact particle detector designed to measure energies and angular distributions of the space radiation environment. Its two detector heads utilize a telescope technique for the spectroscopy of energetic electrons and protons in the energy range required to explore Jupiter's radiation belts. The spectra are given for eight bins equally distributed in the energy log scale. Its third, separated sensor is optimized for measurements of the linear energy transfer from heavy-ions depositions. RADEM can also detect the angular distribution of the incoming radiation with a specially designed pixelated Si-sensor that covers 30% of the sky. A dedicated radiation-hard ASIC is used for RADEM readout electronics, enabling it to cope with extremes of Jupiter's icy-moon surroundings, such as very large fluxes and energies of particles and hazardous radiation levels.

RADEM design was supported with precise computer modeling and extensive calibrations. Proton and electron test facilities used energy spectra and fluxes, as anticipated for operations in space. This resulted in a detailed characterization of the instrument, allowing for the optimization of its final detection scheme and settings and the generation of realistic response functions.

The instrument flies onboard the ESA JUICE mission that was launched on April 14th, 2023. It belongs to the spacecraft platform with the advantage of being fully operational during the eight-year-long cruise phase to the giant planet. This makes RADEM a valuable instrument for Space Weather monitoring in the interplanetary space between Venus and Mars (6 years) and Mars and Jupiter (2 years). RADEM will study SEP and Forbush decreases during the maximum of the 25th Solar Cycle. Together with other instruments on different spacecraft, it will provide crucial data for a better understanding the solar system

radiation environment spectroscopy and its propagation mechanisms. During the nominal operation in the Jupiter magnetosphere, RADEM will not only serve as a radiation monitor but will also provide scientific data that complement observations of the PEP suite with high-energy extensions.

RADEM will undergo regular validation checks and in-space calibrations to ensure its constant performance during the mission. The procedures were tested during its commissioning and will be applied periodically at regular intervals. Further, internal cross-calibrations with the PEP instruments will be performed in the future Lunar Earth Gravitational Assist phase. In addition, its sensors will be validated during the JUICE passage through the Earth's radiation belts. RADEM has already started continuously measuring the radiation environments in the Solar System. Its stable performance provided the first data of CR and several SEPs. The results look very promising both with respect to the analysis of solar event mechanisms and in anticipation of the main RADEM goal of accurately characterizing the Jupiter dynamic radiation environment.

**Author Contribution** PG, MP, PS, RM, HX, FS, LA, AG, AMa, TAS, DM, BSC, ER, GS, SV, OW, PN, NA, LD, AMe, IR, MV, TR, AMr contributed equally to this work.

**Funding Information** Open Access funding provided by Lib4RI - Library for the Research Institutes within the ETH Domain: Eawag, Empa, PSI & WSL. W.H. and A.G. acknowledge funding through PRODEX project 4000142479. B.S.-C. acknowledge support through UK-STFC Ernest Rutherford Fellowship ST/V004115/1. PSI team would also like to thank our HIPA and accelerator groups for their support and free access to the particle facilities. E.R. acknowledges the support of the German Space Agency DLR through contracts 50 QJ 1301, 50 QJ 1503, 50 QJ 2303. Data in Fig. 32 are a product of the ESA-funded project FIRESPELL (ESA contract no. 4000142510/23/NL/CRS), led by SPARC/Greece, provided with permission. Any figures using JUICE ephemeris or pointing information are based on the mission's SPICE kernels, and specifically trajectory 5.1 150lb23.1 (https://www.cosmos.esa.int/web/spice/spice-for-juice). IDEAS acknowledges the support from ESA (4000110643 and 4000104778), the Norwegian Space Centre (BAS.04.13.1), and the Research Council of Norway (Industrial-PhD 254678).

## Declarations

**Competing Interests** The authors declare no competing interests.



## References

Addison P, Liuzzo L, Simon S (2023) Surface-plasma interactions at Europa in draped magnetospheric fields: the contribution of energetic electrons to energy deposition and sputtering. J Geophys Res Space Phys 128(8):e2023JA031734. https://doi.org/10.1029/2023JA031734

Agostinelli S, et al (2003) GEANT4-a simulation toolkit. Nucl Instrum Methods Phys Res, Sect A, Accel Spectrom Detect Assoc Equip 506:250. https://doi.org/10.1016/S0168-9002(03)01368-8

Allen JAV, Randall BA, et al (1975) Pioneer 11 observations of energetic particles in the jovien magnetosphere. Science 188:329–354

Anglin JD, Burrows JR, Mu JL, Wilson MD (1992) Trapped energetic ions in Jupiter's inner magnetosphere. J Geophys Res 102(A1):1–36

Atwell W, Townsend L, Miller T, Campbell C (2005) A reassessment of Galileo radiation exposures in the Jupiter magnetosphere. Radiat Prot Dosim 116(1–4):220–223
Bagenal F, Wilson RJ, Siler S, Paterson WR, Kurth WS (2016) Survey of Galileo plasma observations in Jupiter's plasma sheet. J Geophys Res Planets 121(5):871–894. https://doi.org/10.1002/2016JE005009
Baker DN, Allen JAV (1977) Revised pioneer 10 absolute electron intensities in the inner Jovian magnetosphere. J Geophys Res, Atmos 82:681–683
Barabash S, et al (2025) Particle Environment Package (PEP). Space Sci Rev 221
Bolton SJ (2017) The JUNO mission. Space Sci Rev 213:5–37. https://doi.org/10.1007/s11214-017-0429-6
Bolton SJ, Bagenal F, Blanc M, Cassidy T, Chané E, Jackman C, Jia X, et al (2015) Jupiter's magnetosphere: plasma sources and transport. Space Sci Rev 192:209. https://doi.org/10.1007/s11214-015-0184-5
CCMC (2024) Community Coordinated Modeling Center (CCMC) at Goddard Space Flight Center. https://kauai.ccmc.gsfc.nasa.gov/DONKI/view/FLR/29062/6
Clark G, Tao C, Mauk BH, Nichols J, Saur J, Bunce EJ, Allegrini F, et al (2018) Precipitating electron energy flux and characteristic energies in Jupiter's main auroral region as measured by Juno/JEDI. J Geophys Res Space Phys 123(9):7554–7567. https://doi.org/10.1029/2018JA025639
Cohen CMS, Stone EC, Selesnick RS (2001) Energetic ion observations in the middle Jovian magnetosphere. J Geophys Res 106:29871–29882. https://doi.org/10.1029/2001JA000008
Conlon TF (1978) The interplanetary modulation and transport of Jovian electrons. J Geophys Res 83:541–552. https://doi.org/10.1029/JA083iA02p00541
del Peral L, Gomez-Herrero R, Rodriguez-Frias MD, Gutierrez J, Müller-Mellin R, Kunow H (2003) Jovian electrons in the heliosphere: new insights from EPHIN on board SOHO. Astropart Phys 20(2):235–245. https://doi.org/10.1016/S0927-6505(03)00170-1
Desorgher L, Hajdas W, Britvitch I, Egli K, Guo X, Luo Y, Chastellain F, et al (2013) The Next Generation Radiation Monitor- NGRM. In: 2013 IEEE Nuclear Science Symposium and Medical Imaging Conference (2013 NSS/MIC), pp 1–6. https://doi.org/10.1109/NSSMIC.2013.6829497
Dialynas K, Krimigis SM, Decker RB, Hill M, Mitchell DG, Hsieh KC, Hilchenbach M, Czechowski A (2022) The structure of the global heliosphere as seen by in-situ ions from the Voyagers and remotely sensed ENAs from Cassini. Space Sci Rev 218(21):1572. https://doi.org/10.1007/s11214-022-00889-0
Divine N, Garret H.B., (2009) Worst Case Jupiter Radiation Environment According to 3 Existing Models (Divine-Garrett, GIRE and Salammbo-3D) Technical Report. Noordwijk, NL: European Space Research; Technology Centre
Dougherty M, et al (2025) The JUICE Magnetometer (J-MAG). Space Sci Rev 221
Enghoff MB, Svensmark J, Becker HN, Jørgensen JL, Kotsiaros S, Herceg M, Alexander JW, Florence MM, Connerney JEP (2024) Cutoff rigidities, galactic cosmic ray flux, and heavy ion detections at Jupiter. J Geophys Res Planets 129(2):e2023JE008085. https://doi.org/10.1029/2023JE008085
Fieseler PD, Ardalan SM, Frederickson AR (2002) The radiation effects on Galileo spacecraft systems at Jupiter. IEEE Trans Nucl 49(6):2739–2758
Fletcher L, et al (2023) Jupiter science enabled by ESA's JUpiter ICy moons Explorer. Space Sci Rev 219:53. https://doi.org/10.1007/s11214-023-00996-6
Galli A, Vorburger A, Carberry Mogan SR, Roussos E, Stenberg Wieser G, Wurz P, Föhn M, et al (2022) Callisto's atmosphere and its space environment: prospects for the particle environment package on board JUICE. Earth Space Sci 9(5):e02172. https://doi.org/10.1029/2021EA002172
Giacalone J, Fahr H, Fichtner H, Florinski V, Heber B, Hill ME, Kóta J, Leske RA, Potgieter MS, Rankin JS (2022) Anomalous cosmic rays and heliospheric energetic particles. Space Sci Rev 218(22):1572. https://doi.org/10.1007/s11214-022-00890-7
Gieseler J, Dresing N, Palmroos C, Freiherr von Forstner JL, Price DJ, Vainio R, Kouloumvakos A, et al (2023) Solar-MACH: an open-source tool to analyze solar magnetic connection configurations. Front Astron Space Sci 9. https://doi.org/10.3389/fspas.2022.1058810
Grasset O, Dougherty MK, Coustenis A, Bunce EJ, Erd C, Titov D, Blanc M, et al (2013) JUpiter ICy moons Explorer (JUICE): an ESA mission to orbit Ganymede and to characterise the Jupiter system. Planet Space Sci 78:1–21. https://doi.org/10.1016/j.pss.2012.12.002
Hajdas W, Bühler P, Eggel C, Favre P, Mchedlishvili A, Zehnder A (2003) Radiation environment along the INTEGRAL orbit measured with the IREM monitor. Astron Astrophys 411(1):L43–L47. https://doi.org/10.1051/0004-6361:20031251
Hajdas W, Gonçalves P, Galli A, Marcinkowski R, Arruda L, Santos F, Xiao H, et al (2023) The Radiation Monitor Onboard JUICE: Science Case During Cruise. Heliophysics in Europe Workshop, November 2023, Organized by ESA
Halekas JS, Lin RP, Mitchell DL (2005) Large negative lunar surface potentials in sunlight and shadow. Geophys Res Lett 32:L09102. https://doi.org/10.1029/2005GL022627
Hao Y-X, Sun Y-X, Roussos E, Liu Y, Kollmann P, Yuan C-J, Krupp N, et al (2020) The formation of Saturn's and Jupiter's electron radiation belts by magnetospheric electric fields. Astrophys J Lett 905:L10. https://doi.org/10.3847/2041-8213/abca3f

Herceg M, Jørgensen JL, Merayo JMG, Denver T, Jørgensen PS, Benn M, Kotsiaros S, Connerney JEP, Bolton SJ (2022) Energetic electron lensing caused by Ganymede's magnetic field. Planet Space Sci 224:105597. https://doi.org/10.1016/j.pss.2022.105597

Hill ME, Allen RC, Kollmann P, Brown LE, Decker RB, McNutt RL, Krimigis SM, Andrews GB, Bagenal F, Clark G, Elliott HA, Jaskulek SE, Kusterer MB, Leske RA, Lisse CM, Mewaldt RA, Nelson KS, Richardson JD, Romeo G, Salazar NA, Vandegriff JD, Bernardoni EA, Gladstone GR, Horanyi M, Linscott IR, Singer KN, Steffl AJ, Summers ME, Throop HB, Young LA, Olkin CB, Parker JWm, Spencer JR, Stern SA, Verbiscer AJ, Weaver HA (2020) Influence of solar disturbances on galactic cosmic rays in the solar wind, heliosheath, and local interstellar medium: advanced composition explorer, new horizons, and Voyager observations. Astrophys J 906(1):69. https://doi.org/10.3847/1538-4357/abb408

Honig T, Witasse OG, Evans H, Nieminen P, Kuulkers E, Taylor MGGT, Heber B, Guo J, Sánchez-Cano B (2019) Multi-point galactic cosmic ray measurements between 1 and 4.5 AU over a full solar cycle. Ann Geophys 37(5):903–918. https://doi.org/10.5194/angeo-37-903-2019

Hualin X (2022) g4cad - A freecad workbench for converting CAD files to gdml (v1.0). Zenodo. https://doi.org/10.5281/zenodo.7085915

Hussmann H, Palumbo P, Jaumann R, Dougherty M, Langevin Y, Piccioni G, Barabash S, et al (2014) JUICE JUpiter ICy Moons Explorer – Exploring the Emergence of Habitable Worlds Around Gas Giants Around Gas Giants. European Space Agency Definition Study Report: ESA/SRE(2014)1

Integrated Detector Electronics AS IDEAS (2025) https://ideas.no/

Jun I, Garrett HB, Evans RW (2005) High-energy trapped particle environments at Jupiter: an update. IEEE Trans Nucl Sci 52(6):2281–2286. https://doi.org/10.1109/TNS.2005.860747

Khurana KK, Kivelson MG, Vasyliunas VM, Krupp N, Woch J, Lagg A, Mauk BH, Kurth WS (2004) The configuration of Jupiter's magnetosphere. In: Bagenal F, Dowling TE, McKinnon WB (eds) Jupiter: The planet, satellites and magnetosphere. Cambridge University Press, pp 593–616

Kivelson MG, Bagenal F, Kurth WS, Neubauer FM, Paranicas C, Saur J (2004) Magnetospheric interactions with satellites. In: Jupiter: the planet, satellites and magnetosphere, pp 513–536

Kollmann P, Paranicas C, Clark G, Roussos E, Lagg A, Krupp N (2016) The vertical thickness of Jupiter's Europa gas torus from charged particle measurements. Geophys Res Lett 43:9425–9433. https://doi.org/10.1002/2016GL070326

Kollmann P, Roussos E, Paranicas C, Woodfield EE, Mauk BH, Clark G, Smith DC, Vandegriff J (2018) Electron acceleration to MeV energies at Jupiter and Saturn. J Geophys Res Space Phys 123(11):9110–9129. https://doi.org/10.1029/2018JA025665

Krupp N, Dougherty MK, Woch J, Seidel R, Keppler E (1999) Energetic particles in the duskside Jovian magnetosphere. J Geophys Res 104(A7):14767–14780. https://doi.org/10.1029/1999JA900156

Krupp N, Roussos E, Fränz M, Kollmann P, Paranicas C, Clark G, Khurana K, Galli A (2023) Pitch angle distributions of energetic particles near Callisto. J Geophys Res Space Phys 128(10):e2023JA031794. https://doi.org/10.1029/2023JA031794

Kuulkers E, Ferrigno C, Kretschmar P, Alfonso-Garzón J, Baab M, Bazzano A, Bélanger G, et al (2021) INTEGRAL reloaded: spacecraft, instruments and ground system. New Astron Rev 93:101629. https://doi.org/10.1016/j.newar.2021.101629

Liu Z-Y, Zong Q-G, Blanc M, Sun Y-X, Zhao J-T, Hao Y-X, Mauk BH (2021) Statistics on Jupiter's current sheet with Juno data: geometry, magnetic fields and energetic particles. J Geophys Res Space Phys 126(11):e29710. https://doi.org/10.1029/2021JA029710

Liuzzo L, Poppe AR, Nénon Q, Simon S, Addison P (2024) Constraining the influence of Callisto's perturbed electromagnetic environment on energetic particle observations. J Geophys Res Space Phys 129(2):e2023JA032189. https://doi.org/10.1029/2023JA032189

Ma Q, Li W, Zhang X-J, Shen X-C, Daly A, Bortnik J, Mauk BH, et al (2021) Energetic electron distributions near the magnetic equator in the Jovian plasma sheet and outer radiation belt using Juno observations. Geophys Res Lett 48:e95833. https://doi.org/10.1029/2021GL095833

Matthiä D, Hassler DM, de Wet W, Ehresmann B, Firan A, Flores-McLaughlin J, Guo J, et al (2017) The radiation environment on the surface of Mars - summary of model calculations and comparison to RAD data. Life Sci Space Res 14:18–28. https://doi.org/10.1016/j.lssr.2017.06.003

Melin H, O'Donoghue J, Moore L, Stallard TS, Fletcher LN, Roman MT, Harkett J, King ORT, Thomas EM, Wang R, Tiranti PI, Knowles KL, de Pater I, Fouchet T, Fry PH, Wong MH, Holler BJ, Hueso R, James MK, Orton GS, Mura A, Sánchez-Lavega A, Lellouch E, de Kleer K, Showalter MR (2024) Ionospheric irregularities at Jupiter observed by JWST. Nat Astron 8(8):1000–1007. https://doi.org/10.1038/s41550-024-02305-9

Mohammadzadeh A, Evans H, Nieminen P, Daly E, Vuilleumier P, Buhler P, Eggel C, et al (2003) The ESA standard radiation environment monitor program first results from PROBA-1 and INTEGRAL. IEEE Trans Nucl Sci 50(6):2272–2277. https://doi.org/10.1109/TNS.2003.821796

Nénon Q, Sicard A, Kollmann P, Garrett HB, Sauer SPA, Paranicas C (2018) A physical model of the proton radiation belts of Jupiter inside Europa's orbit. J Geophys Res Space Phys 123(5):3512–3532. https://doi.org/10.1029/2018JA025216

Nenon Q, Miller LP, Kollman P, Liuzzo L, Pinto M, Witasse O (2022) Pitch angle distribution of MeV electrons in the magnetosphere of Jupiter. J Geophys Res 127(8):e2022JA030627. https://doi.org/10.1029/2022JA030627

Nordheim TA, Jasinski JM, Hand KP (2019) Galactic cosmic-ray bombardment of Europa's surface. Astrophys J Lett 881:L29. https://doi.org/10.3847/2041-8213/ab3661

Odenwald S, Green J, Taylor W (2006) Forecasting the impact of an 1859-calibre superstorm on satellite resources. Adv Space Res 38(2):280–297. https://doi.org/10.1016/j.asr.2005.10.046

Pinto M (2019) Development of a Directionality Detector and Radiation Hardness Assurance for RADEM, the ESA JUICE Mission Radiation Monitor. PhD thesis. Instituto Superior Técnico - University of Lisbon

Pinto M, Gonçalves P (2019) GUIMesh: a tool to import STEP geometries into Geant4 via GDML. Comput Phys Commun 239:150–156. https://doi.org/10.1016/j.cpc.2019.01.024

Pinto M, Sanchez-Cano B, Moissl R, Benkhoff J, Cardoso C, Gonçalves P, Assis P, et al (2017) The BepiColombo Environment Radiation Monitor, BERM. Space Sci Rev 218(7):54. https://doi.org/10.1007/s11214-022-00922-2

Pinto M, Gonçalves P, Socha P, Hajdas W, Marques A, Pinto C (2019a) Beam test results of RADEM engineering model. Nucl Instrum Methods Phys Res. https://doi.org/10.1016/j.nima.2019.162795

Pinto M, Goncalves P, Wojtek H, Marques A, Pinto JC (2019b) Development of a directionality detector for RADEM, the radiation hard electron monitor aboard the JUICE mission. IEEE Trans Nucl Sci 66(7):1770–1777. https://doi.org/10.1109/TNS.2019.2900398

Plainaki C, Cassidy TA, Shematovich VI, Milillo A, Wurz P, Vorburger A, Roth L, et al (2018) Towards a global unified model of Europa's tenuous atmosphere. Space Sci Rev 214:40. https://doi.org/10.1007/s11214-018-0469-6

Potgieter MS (2017) The global modulation of cosmic rays during a quiet heliosphere: a modeling perspective. Adv Space Res 60(4):848–864. https://doi.org/10.1016/j.asr.2016.09.003

Raghav A, Shaikh Z, Bhaskar A, Datar G, Vichare G (2017) Forbush decrease: a new perspective with classification. Sol Phys 292:99. https://doi.org/10.1007/s11207-017-1121-4

Roussos E, Andriopoulou M, Krupp N, Kotova A, Paranicas C, Krimigis SM, Mitchell DG (2013) Numerical simulation of energetic electron microsignature drifts at Saturn: methods and applications. Icarus 226:1595–1611. https://doi.org/10.1016/j.icarus.2013.08.023

Roussos E, Jackman CM, Thomsen MF, Kurth WS, Badman SV, Paranicas C, Kollmann P, et al (2018a) Solar Energetic Particles (SEP) and Galactic Cosmic Rays (GCR) as tracers of solar wind conditions near Saturn: event lists and applications. Icarus 300:47–71. https://doi.org/10.1016/j.icarus.2017.08.040

Roussos E, Kollmann P, Krupp N, Paranicas C, Dialynas K, Sergis N, Mitchell DG, Hamilton DC, Krimigis SM (2018b) Drift-resonant, relativistic electron acceleration at the outer planets: insights from the response of Saturn's radiation belts to magnetospheric storms. Icarus 305:160–173. https://doi.org/10.1016/j.icarus.2018.01.016

Roussos E, Dialynas K, Krupp N, Kollmann P, Paranicas C, Roelof EC, Yuan C, Mitchell DG, Krimigis SM (2020) Long- and short-term variability of galactic cosmic-ray radial intensity gradients between 1 and 9.5 au: observations by Cassini, BESS, BESS-Polar, PAMELA, and AMS-02. Astrophys J 904(2):165. https://doi.org/10.3847/1538-4357/abc346

Roussos E, Allanson O, André N,et al (2022) The in-situ exploration of Jupiter's radiation belts. Exp Astron 54:745–789. https://doi.org/10.1007/s10686-021-09801-0

Sandberg I, Aminalragia-Giamini S, Papadimitriou C, Van Gijlswijk R, Heynderickx D, Marcinkowski R, Hajdas W, Heil M, Evans H (2022) First results and analysis from ESA next generation radiation monitor unit on-board EDRS-C. IEEE Trans Nucl Sci 69(7):1549–1556. https://doi.org/10.1109/TNS.2022.3160108

Santos-Costa D, Bourdarie SA (2001) Modeling the inner Jovian electron radiation belt including non-equatorial particles. Planet Space Sci 49:303–312. https://doi.org/10.1016/S0032-0633(00)00151-3

Selesnick RS (2002) Cosmic ray access to Jupiter's magnetosphere. Geophys Res Lett 29:1298. https://doi.org/10.1029/2001GL014146

Selesnick RS, Albert JM (2019) Variability of the proton radiation belt. J Geophys Res Space Phys 124(7):5516–5527. https://doi.org/10.1029/2019JA026754

Selesnick RS, Cohen CMS, Khurana KK (2001) Energetic ion dynamics in Jupiter's plasma sheet. J Geophys Res 106:18895–18906. https://doi.org/10.1029/2000JA000242

Socha P (2021) Qualification of the RADEM instrument for the ESA JUICE Mission. PhD thesis. ETH, Zurich

Stein TA, et al (2016) Front-end readout ASIC for charged particle counting with the RADEM instrument on the ESA JUICE mission. Proc SPIE 9905:990546. https://doi.org/10.1117/12.2231901

Strauss RD, Potgieter MS, Büsching I, Kopp A (2011) Modeling the modulation of galactic and Jovian electrons by stochastic processes. Astrophys J 735(2):83. https://doi.org/10.1088/0004-637X/735/2/83

Strauss RD, Dresing N, Engelbrecht NE, Mitchell JG, Kühl P, Jensen S, Fleth S, et al (2024) Jovian electrons in the inner heliosphere: opportunities for multi-spacecraft observations and modeling. Astrophys J 961(1):57. https://doi.org/10.3847/1538-4357/ad11db

Tomás A, Woch J, Krupp N, Lagg A, Glassmeier K-H, Dougherty MK, Hanlon PG (2004) Changes of the energetic particles characteristics in the inner part of the Jovian magnetosphere: a topological study. Planet Space Sci 52:491–498. https://doi.org/10.1016/j.pss.2003.06.011

Trumbo SK (2021) Views of an Ocean World: the Signatures of Internal and External Processes on the Surface of Europa. PhD thesis. California Institute of Technology, Division of Geological; Planetary Sciences

Trumbo SK, Brown ME, Hand KP (2019) $H_2O_2$ within chaos terrain on Europa's leading hemisphere. Astron J 158:127. https://doi.org/10.3847/1538-3881/ab380c

Vogt A, Heber B, Kopp A, Potgieter MS, Strauss RD (2018) Jovian electrons in the inner heliosphere. Proposing a new source spectrum based on 30 years of measurements. Astron Astrophys 613:A28. https://doi.org/10.1051/0004-6361/201731736

Vorburger A, Pfleger M, Lindkvist J, Holmström M, Lammer H, Lichtenegger HIM, Galli A, Rubin M, Wurz P (2019) Three-dimensional modeling of Callisto's surface sputtered exosphere environment. J Geophys Res Space Phys 124(8):7157–7169. https://doi.org/10.1029/2019JA026610

Vorburger A, Fatemi S, Carberry Mogan SR, Galli A, Liuzzo L, Poppe AR, Roth L, Wurz P (2024) 3D Monte-Carlo simulation of Ganymede's atmosphere. Icarus 409:115847. https://doi.org/10.1016/j.icarus.2023.115847

Wahlund JE, Bergman JES, Åhlén L, et al (2025) The Radio & Plasma Wave Investigation (RPWI) for the JUpiter ICy moons Explorer (JUICE). Space Sci Rev 221:1. https://doi.org/10.1007/s11214-024-01110-0

Williams DJ (2001) Ganymede's ionic radiation belts. Geophys Res Lett 28:3793–3796. https://doi.org/10.1029/2001GL013353

Williams DJ, et al (1992) The Galileo energetic particle detector. Space Sci Rev 60:385–412. https://doi.org/10.1007/BF00216863

Williams DJ, Mauk B, McEntire RW (1997b) Trapped electrons in Ganymede's magnetic field. Geophys Res Lett 24:2953–2956. https://doi.org/10.1029/97GL03003

Williams DJ, Mauk BH, McEntire RW, Roelof EC, Armstrong TP, Wilken B, Roederer JG, et al (1997a) Energetic particle signatures at Ganymede: implications for Ganymede's magnetic field. Geophys Res Lett 24:2163–2166. https://doi.org/10.1029/97GL01931

Wilson RJ, Vogt MF, Provan G, Kamran A, James MK, Brennan M, Cowley SWH (2023) Internal and external Jovian magnetic fields: community code to serve the magnetospheres of the outer planets community. Space Sci Rev 219:15. https://doi.org/10.1007/s11214-023-00961-3

Witasse O, Sánchez-Cano B, Mays ML, Kajdič P, Opgenoorth H, Elliott HA, Richardson IG, et al (2017) Interplanetary coronal mass ejection observed at STEREO-a, Mars, comet 67P/Churyumov-Gerasimenko, Saturn, and New Horizons en route to Pluto: comparison of its Forbush decreases at 1.4, 3.1, and 9.9 AU. J Geophys Res Space Phys 122(8):7865–7890. https://doi.org/10.1002/2017JA023884

Witasse O, Altobelli N, Martinez S, Lim T, Oliveira J.S., Cornet Y, (2023) JUICE Science Data Generation, Validation and Archiving Plan. Technical Report. Noordwijk, NL: European Space Research; Technology Centre

Yuan C, Zuo Y, Roussos E, Wei Y, Hao Y, Sun Y, Krupp N (2021) Large-scale episodic enhancements of relativistic electron intensities in Jupiter's radiation belt. Earth Planet Phys 5(4):314–326. https://doi.org/10.26464/epp2021037

Yuan C, Roussos E, Wei Y, Krupp N, Liu Z, Wang J (2024) Galileo observation of electron spectra dawn-dusk asymmetry in the middle Jovian magnetosphere: evidence for convection electric field. Geophys Res Lett 51:e2023GL105503. https://doi.org/10.1029/2023GL105503

Zeitlin C, Hassler DM, Cucinotta FA, Ehresmann B, Wimmer-Schweingruber RF, Brinza DE, Kang S, et al (2013) Measurements of energetic particle radiation in transit to Mars on the Mars Science Laboratory. Science 340(6136):1080–1084. https://doi.org/10.1126/science.1235989

## Authors and Affiliations

**Wojtek Hajdas[1] · Patrícia Gonçalves[2,3] · Marco Pinto[4] · Patryk Socha[1,5] · Radoslaw Marcinkowski[1] · Hualin Xiao[1] · Francisca Santos[2,3] · Luísa Arruda[2] · André Galli[6] · Arlindo Marques[7] · Timo A. Stein[8,9] · Dirk Meier[8] · Beatriz Sánchez-Cano[10] · Elias Roussos[11] · Giovanni Santin[4] · Sam Verstaen[4] · Olivier Witasse[4] · Petteri Nieminen[4] · Nicolas Altobelli[12] · Laurent Desorgher[13] · Alessandra Menicucci[14] · Ingo Reinaecker[1] · Marina Vogiatzi[1] · Tigran Rostomyan[1] · Alankritaa Mrigatshi[15]**

✉ W. Hajdas
wojtek.hajdas@psi.ch

P. Gonçalves
patricia@lip.pt

M. Pinto
Marco.Pinto@esa.int

P. Socha
patryk.socha@psi.ch; patryk.socha@hiqt.ch

R. Marcinkowski
radoslaw.marcinkowski@se2s.ch

H. Xiao
hualin.xiao@fhnw.ch

F. Santos
francisca.f.santos@tecnico.ulisboa.pt

L. Arruda
luisa@lip.pt

A. Galli
andre.galli@unibe.ch

A. Marques
arlindo.marques@efacec.com

T.A. Stein
timo.stein@ideas.no

D. Meier
dirk.meier@ideas.no

B. Sánchez-Cano
bscmdr1@leicester.ac.uk

E. Roussos
roussos@mps.mpg.de

G. Santin
Giovanni.Santin@esa.int

S. Verstaen
Sam.Verstaen@esa.int

O. Witasse
Olivier.Witasse@esa.int

P. Nieminen
Petteri.Nieminen@esa.int

N. Altobelli
Nicolas.Altobelli@esa.int

L. Desorgher
laurent.desorgher@chuv.ch

A. Menicucci
A.Menicucci@tudelft.nl

I. Reinaecker
ingo.reinacker@psi.ch

M. Vogiatzi
stella.vogiatzi@psi.ch

T. Rostomyan
tigran.rostomyan@psi.ch

A. Mrigatshi
alankrita.i.mG@gmail.com

1 NUM, Paul Scherrer Institut, Forschungstrasse 111, Villigen PSI, 5232, AG, Switzerland

2 LIP, Laboratory for Instrumentation and Experimental Particle Physics, Av. Prof. Gama Pinto 2, Lisbon, 1649-003, Portugal

3 IST, Instituto Superior Técnico, Lisbon University, Av. Rovisco Pais, Lisbon, 1049-001, Portugal

4 ESTEC, European Space Agency, Keplerlaan 1, 2201 AZ, Noordwijk, The Netherlands

5 Present address: HIQT GmbH, Rheinfelden, Switzerland

6 Space Research and Planetary Sciences, Physics Institute, University of Bern, Hochschulstrasse 4, 3012, Bern, Switzerland

7 EFACEC, Via de Francisco Sá Carneiro Apartado 3078, 4471-907, Moreira da Maia, Portugal

8 Integrated Detector Electronics AS – IDEAS, Gjerdrums vei 19, 0484, Oslo, Norway

9 Department of Physics, University of Oslo, Sem Sælands vei 24, 0371, Oslo, Norway

10 School of Physics and Astronomy, University of Leicester, University road, Leicester, LE1 7RH, UK

11 Max Planck Institute for Solar System Research, Justus-von-Liebig-Weg 3, 37077, Göttingen, Germany

12 ESAC, European Space Agency, Camino bajo del Castillo, s/n, Urbanización Villafranca del Castillo, Villanueva de la Cañada, 28692, Madrid, Spain

13 Institute of Radiation Physics, Lausanne University Hospital and University of Lausanne, 1015, Lausanne, Switzerland

14 TU Delft, Mekelweg 5, 2628 CD, Delft, The Netherlands

15 Thales Alenia Space, Schaffhauserstrasse 580, CH-8052, Zurich, Switzerland